International Journal of Steel Structures
https://doi.org/10.1007/s13296-021-00508-8

Online ISSN 2093-6311
Print ISSN 1598-2351

Optimization of the Double Reduced Beam Section (DRBS) Connection

Saeed Asil Gharebaghi[1] · Reza Fami Tafreshi[1] · Nader Fanaie[1] · Omid Sepasgozar Sarkhosh[2]

Received: 3 February 2021 / Accepted: 17 June 2021

Abstract
The double reduced beam section (DRBS) connection is a newly developed steel moment connection. In this paper, the chaotic particle swarm optimization technique was utilized to optimize this connection for the best seismic performance. The resulting optimum DRBS connection shapes showed up to 39% better energy dissipation and up to respectively 50% and 55% lower rupture index (*RI*) and equivalent plastic strain (*PEEQ*) at the beam-column interface, compared to the conventional RBS connection. Also, the optimum design parameters determined in this paper led to up to a 28% increase in the objective function (energy dissipation) and up to respectively 36% and 38% decreases in the *RI* and *PEEQ* with respect to the original DRBS connection, indicating noticeable seismic performance enhancements. The results indicated that changing the size of the beam and column sections does not lead to any significant change in the optimal shape of the beam flange cut or the seismic performance of the connection.

Keywords Reduced beam section · Chaotic particle swarm optimization · Finite element modeling · Seismic performance · Plastic hinge

List of Symbols

a	The distance between the column face and the start of the reduced section in the RBS connection
a_1	The distance between the column face and the start of the first reduced section in the DRBS connection
a_2	The distance between the column face and the start of the second reduced section in the DRBS connection
A_{web}	Area of the beam web
b	Length of the reduced section in the RBS connection
b_1	Length of the first reduced section in the DRBS connection
b_2	Length of the second reduced section in the DRBS connection
b_{bf}	Beam flange width
b_c	Box-column section width
B	The rate of change in the yield surface
c	Depth of the reduced section in the RBS connection
c_1	Depth of the first reduced section in the DRBS connection
c_2	Depth of the second reduced section in the DRBS connection
C	Modulus of initial kinematic hardening
C_1	First learning (acceleration) factor in CPSO
C_2	Second learning (acceleration) factor in CPSO
C_{pr}	Factor to account for peak connection strength
C_v	Web shear coefficient
d	Distance between the two reduced sections in the DRBS connection
$E(t)$	Area of the individual hysteresis loop without the penalty function applied at time t
$\bar{E}(t)$	Area of the individual hysteresis loop with the penalty function applied at time t

✉ Saeed Asil Gharebaghi
asil@kntu.ac.ir

Reza Fami Tafreshi
rezaft50@yahoo.com

Nader Fanaie
fanaie@kntu.ac.ir

Omid Sepasgozar Sarkhosh
omid.sepasgozar@gmail.com

[1] Department of Civil Engineering, Faculty of Civil Engineering, K. N. Toosi University of Technology, No. 1346, Valiasr St., P.O. Box 15875-4416, Tehran, Iran

[2] Department of Civil Engineering, Faculty of Engineering, University of Guilan, Rasht, Iran

Published online: 26 June 2021

F	Objective function
F_y	Yield strength
H_{beam}	Beam section depth
$iter$	Current number of iterations
$iter_{max}$	Maximum number of iterations
L	Beam length
L_b	Beam half-length
M_f	Maximum moment at the column face
M_{pb}	Nominal plastic flexural strength of the beam
M_{pc}	Nominal plastic flexural strength of the column
M_{pr}	Probable maximum moment at the plastic hinge location
M_{pr1}	Probable maximum moment at the first reduced section
M_{pr2}	Probable maximum moment at the second reduced section
p	Hydrostatic stress
$p_{b,i}(t)$	Personal best value of the ith particle at time t
$p_g(t)$	Global best value at time t
P_c	Available axial compressive strength
$P(t)$	Penalty function value at time t
$PEEQ$	Equivalent plastic strain
q	Von Mises stress
Q	Largest change in the size of the yield surface
$r_{1,i}$	First random number series in CPSO
$r_{2,i}$	Second random number series in CPSO
R_n	Nominal strength of the panel zone in the elastic state
R_y	Yield strength factor
RI_{final}	Rupture index in the equivalent non-RBS connection
RI_{max}	Desired upper limit for the rupture index
RI	Rupture index
$RI(t)$	Maximum rupture index value at time t
T	Time
t_c	Box-column section thickness
t_f	Beam flange thickness
t_w	Beam web thickness
$v_i(t)$	Velocity of the ith particle at time t
V_h	Shear force at the plastic hinge location
V_n	Nominal shear strength
$x_i(t)$	Current position of the ith particle at time t
Z_{pb}	Plastic modulus of the beam section
Z_{pc}	Plastic modulus of the column section
γ	The rate of reduction of kinematic hardening
ε_{ij}	Plastic strain components
ε_p	Plastic strain
σ	Stress
σ_y	Yield stress
Φ	Reduction factor
ω	Inertia weight
ω_{min}	Lower limit for the inertia weight
ω_{max}	Upper limit for the inertia weight

1 Introduction

Steel is one of the most important and valuable iron alloys with various applications, ranging from constructing modern steel structures to improving old reinforced concrete structures and preserving the ancient architecture of buildings (Foraboschi, 2016). Steel structures are one of the most common types of structures in the world. Nowadays, evaluating the performance of steel frames has become a common discussion among researchers. These frames are designed and built with various connections, in which the ductility is usually provided through the formation of a bending moment plastic hinge at the ends of the structural beams. In analyzing these frames, loading conditions such as lateral loading, buckling, geometric nonlinearities, and the interaction of axial force and bending moment in the members must be considered (Foraboschi, 2019).

The 1994 Northridge earthquake resulted in widespread and unexpected brittle failures in rigid steel beam-to-column connections that brought the contents of building codes into question (Mahin, 1998; Popov et al., 1998). After this earthquake, one of the significant changes that occurred in the design concept of moment-resisting steel frames was that the plastic hinge must form inside the beam and away from the beam-column interface to increase the ductility of the frames (Chen & Tu, 2004). Two general approaches of strengthening the beam at the beam-column interface and weakening the beam at specific and limited distances from the column face have been proposed to achieve this goal (FEMA 350, 2000). Proposed designs for the strengthened beam approach include widening the beam flanges at the beam-column interface (Chen et al., 2006) and using rib and wing plates (Chen et al., 2004). This approach results in higher costs and problems, such as increased welding and the need for a more robust panel zone. In contrast, the beam weakening approach covers some of the downsides in the strengthening approach (FEMA 350, 2000).

Different designs have been proposed for weakening the beam, the most important of which is the reduced beam section (RBS) connection (Chen & Tu, 2004; Engelhardt et al., 1998). In the RBS connection, a portion of each beam flange is cut in various shapes at a specified distance from the column face. By doing so, the plastic hinge no longer forms in the column, and the intentionally weakened area acts as a ductile structural fuse (El-Bahey & Bruneau, 2012). The formation of the plastic hinge at the reduced section results in less strain and stress demand at the beam-column interface. The beam flanges can be cut in different ways (Uang & Fan, 2001). Comprehensive data on various cut shapes have been presented by Sophianopolus and Deri (2011). In 1990, Plumier proposed the

trapezoidal flange cut profile as the first concept for reducing beam sections (Plumier, 1990). The tapered-cut RBS connection proposed by Chen et al. (1996) and the radius-cut RBS connection proposed by Engelhardt et al. (1998) are among the other design concepts introduced later. Research has shown that among the proposed concepts, the radius-cut RBS connection minimizes stress concentration through a gradual decrease in the flange section. As a result, the risk of brittle connection failure decreases. This design has the highest ductility and the best performance as it distributes plastic deformations along the reduced section and has shown large plastic rotations in experiments conducted (Chen & Tu, 2004; Engelhardt et al., 1998). It has also been shown that this type of connection has a negligible effect on the stiffness of moment-resisting frames (Fanaie et al., 2019). Currently, the radius-cut RBS connection is approved by different international building codes.

Morshedi et al.'s (2017) study proposed a new RBS connection intended to delay web local buckling (WLB), flange local buckling (FLB), and lateral-torsional buckling (LTB) in beams. This moment-resisting connection, shown in Fig. 1, consists of two adjacent radius-cut reduced sections and is hence called the double reduced beam section (DRBS) connection. The additional reduced section works as an auxiliary structural fuse by enabling consecutive redistribution of stress between the two reduced sections, resulting in a wide plastic hinge (Morshedi et al., 2017).

Morshedi et al. (2017), through comparison of the behavior of RBS and DRBS connections, showed that utilizing the DRBS connection delays the strength degradation by allowing for an extra 2% inter-story drift. The main advantage of the DRBS connection over the RBS connection was found to be the reduction of equivalent plastic strain (*PEEQ*) through the balanced distribution of deformations between the two reduced sections. This mechanism delays local failure in these sections. Their results have shown that using the DRBS connection leads to up to a 60% decrease in *PEEQ* at the beam-column interface. In addition to delaying the buckling modes, the involvement of both reduced sections in energy absorption results in a 50% to 75% increase in energy dissipation compared to the RBS connection (Morshedi et al., 2017).

As presented in Fig. 1, proposed specifications for the DRBS connection follow the recommendations of ANSI/AISC 358-16 (2016b) for the RBS connection except for the depth of the second reduced section (c_2), for which no upper limit is recommended. This parameter is the critical design variable for achieving simultaneous plasticization of both reduced sections and hence the best connection performance (Morshedi et al., 2017). There are two limit states for c_2; very small values of this parameter lead to the formation of a single plastic hinge at the first reduced section (as in the RBS connection), and very high values of c_2 result in the formation of a single plastic hinge at the second reduced section. The optimum value for c_2 lies between these two limit states and allows for the balanced formation of plastic hinges at both reduced sections, resulting in decreased *PEEQ*, delayed buckling modes, increased energy dissipation, and less post-earthquake damage.

Morshedi et al. (2017) evaluated 15 sample connections with different cut parameters in their study. Their results

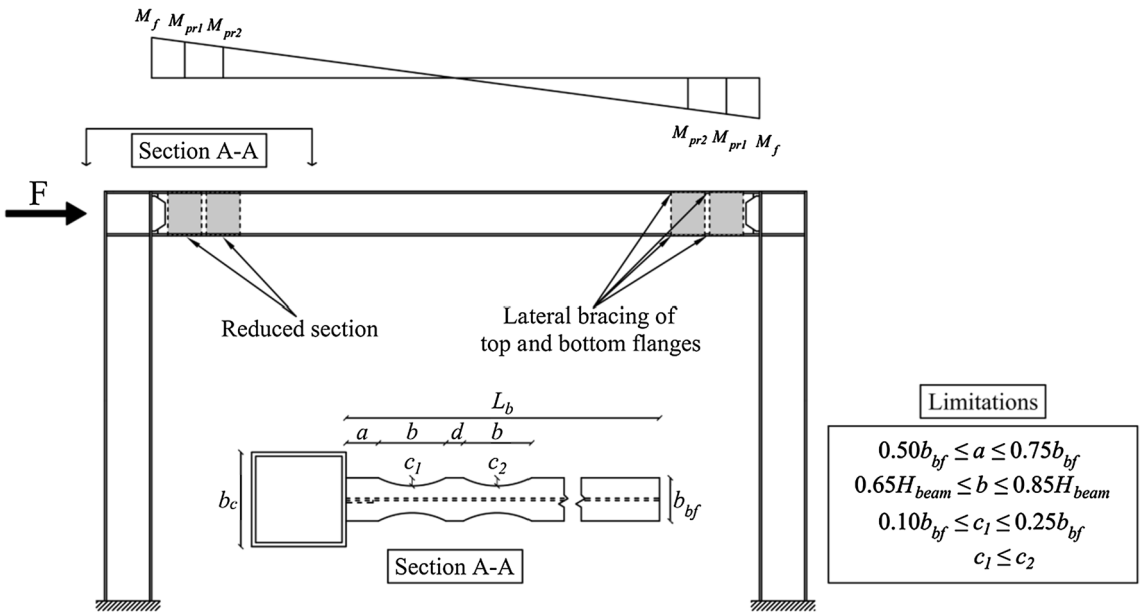

Fig. 1 The DRBS connection proposed by Morshedi et al. (2017)

suggest that DRBS connections with higher b and lower a values provide higher energy dissipation. As shown in Fig. 1, in the proposed specifications, the flange cut length (b) is considered equal for both reduced sections, and there are also no details about the distance between the two reduced sections (d). Given the specifications provided, further investigation of the DRBS connection is still necessary to obtain optimum values for all beam flange cut parameters in this newly developed design.

In this research, for the first time, it was tried to optimize the DRBS connection cut parameters and obtain the optimum shape of this newly proposed steel connection with the aim of achieving greater ductility and energy dissipation and delaying strength degradation under cyclic loading. For this purpose, an optimization engine was developed utilizing the chaotic particle swarm optimization (CPSO) technique and finite element modeling. In order to confirm the accuracy of the developed CPSO engine, and to obtain data for comparison, it was first tested on a conventional RBS connection. The CPSO engine was then utilized to optimize DRBS connections of three different sizes and find the optimum values for all of the cut parameters involved. Based on the results obtained, the seismic performance of the DRBS connection was investigated compared to the conventional RBS connection. Also, the results were employed to evaluate the effect of the beam and column section size on the optimum shape and seismic performance of the DRBS connection.

2 Optimization Method

2.1 PSO and CPSO Algorithms

Particle swarm optimization (PSO) algorithm is a population-based meta-heuristic algorithm first proposed by Eberhart and Kennedy (1995). The PSO algorithm first starts with a group of random solutions called particles. Then, it attempts to find the optimal solution in the given problem space by successively updating the initial particles. The current position and velocity of the ith particle in the problem space at the time t could be represented by the two values $x_i(t)$ and $v_i(t)$, respectively. After each iteration of the population movement, the properties of each particle are updated based on its personal best value and the global best value from all particles, respectively denoted by $p_{b,i}(t)$ and $p_g(t)$, using the following equations:

$$v_i(t+1) = \omega v_i(t) + C_1 r_{1,i}(t)\,(p_{b,i}(t) - x_i(t)) + C_2 r_{2,i}(t)\,(p_g(t) - x_i(t)) \quad (1)$$

$$x_i(t+1) = x_i(t) + v_i(t+1) \quad (2)$$

In the above equations, ω is the inertia weight, C_1 and C_2 are the learning factors or the acceleration coefficients, and $r_{1,i}$ and $r_{2,i}$ are random number series with uniform distribution within the interval (0, 1). Figure 2 schematically illustrates the particle velocity and position update in a two-dimensional vector problem space and the basic concept of the PSO (Kim et al., 2017).

C_1, C_2, and ω are the main parameters of the PSO algorithm. Choosing the appropriate values for these parameters in the PSO algorithm is a vital topic that has been investigated by many researchers. The convergence and performance of this algorithm depend on the values chosen for the above parameters. Usually, C_1 and C_2 are considered to be between 1.5 and 2. In this research, as in several other previously conducted studies, both of these parameters were chosen to be equal to 2. Related studies also suggest that the convergence of the PSO algorithm is strongly dependent on the value of ω, which is the factor responsible for appropriate speed control

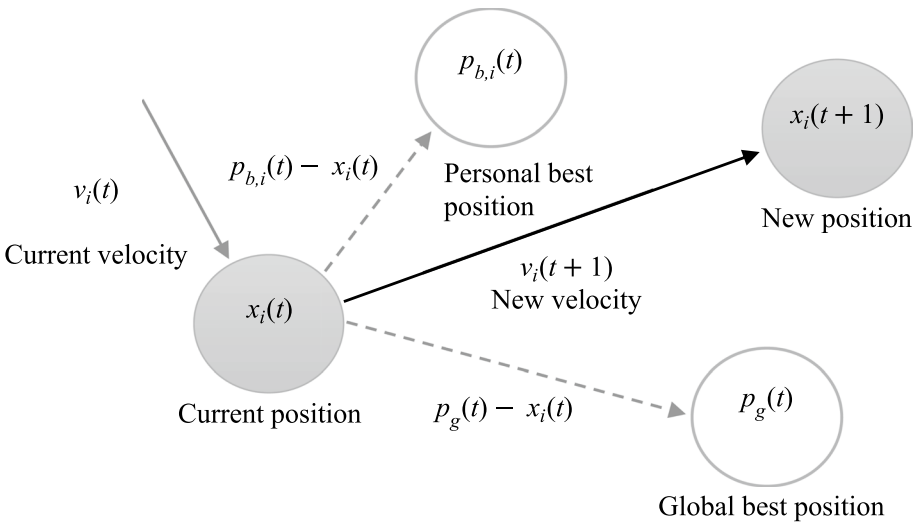

Fig. 2 Basic concept of the PSO (Kim et al., 2017)

in the search for the local and global optimums. It is generally recommended that the value of ω be defined dynamically and linearly reduced during the population evolution process. A large value for ω at the beginning of the process will allow obtaining reasonable solutions in the early stages, and a small value set for the final stages will lead to better convergence (Parsopoulos et al., 2001). Hence, in this study, a dynamic ω with values within the interval (0, 1), defined using Eq. (3), was used during the optimization process. In Eq. (3), ω_{min} and ω_{max} are the lower and upper limits for ω, which were chosen to be equal to 0 and 1. In addition, *iter* and $iter_{max}$ respectively denote the current and the maximum number of iterations.

$$\omega = \omega_{max} - \left(\frac{\omega_{max} - \omega_{min}}{iter_{max}} \right) \times iter \tag{3}$$

While PSO is an effective and highly efficient method for finding the global optimum in a problem space, premature convergence to local optimums is one of its fundamental weaknesses (Shi & Eberhart, 1998). One of the approaches that have been recently proposed to overcome this weakness is utilizing chaotic maps in the PSO algorithm. This method, called chaotic particle swarm optimization (CPSO), allows for a broader and faster search across the problem space and leads to improved results by avoiding local optimums. It also requires less computational effort and system memory, compared to other algorithms such as the genetic algorithm (GA), as does it does not have many operators or parameters. CPSO uses chaotic maps instead of uniform distribution in order to generate the random number series $r_{1,i}$ and $r_{2,i}$ in Eq. (1), which creates variation in the particle population and hence improves the performance by eliminating premature convergence (Altinoz et al., 2010; Dos Santos & Mariani, 2009). The improved performance of the CPSO algorithm has also been previously utilized in the optimal active control of shear buildings (Gharebaghi & Zangooei, 2017). Because of the above-mentioned advantages of the CPSO, it is a suitable technique for optimization problems involving multiple parameters. Hence, this technique was utilized in this paper to optimize the DRBS connection.

In the present study, the logistic map, which is one of the most prominent types of chaotic maps, was used to generate random number series in the CPSO algorithm. The formulations for this algorithm are identical to those developed for the simple PSO algorithm except that random number series $r_{1,i}$ and $r_{2,i}$ in Eq. (1) are generated using logistic chaotic maps based on the following pair of equations:

$$r_{1,i}(t+1) = 4\ r_{1,i}(t)\ (1 - r_{1,i}(t)) \tag{4}$$

$$r_{2,i}(t+1) = 4\ r_{2,i}(t)\ (1 - r_{2,i}(t)) \tag{5}$$

In the first iteration, the values of $r_{1,i}(1)$ and $r_{2,i}(1)$ are arbitrarily chosen numbers between 0 and 1, but in the next iterations, the series values are generated through logistic mapping based on Eqs. (4) and (5) (Gharebaghi & Zangooei, 2017).

2.2 Objective and Penalty Functions

In this study, the total energy dissipated during the cyclic loading, obtained by calculating the total area of the hysteresis loops, was considered as the objective function. To prevent weld fracture and increase ductility, a desired upper limit (RI_{max}) was considered for the rupture index (*RI*) value at the beam-column interface. The rupture index is defined using the equation proposed by El-Tawil et al. (1999):

$$RI = \frac{PEEQ}{\exp\left(-1.5\,\frac{p}{q}\right)} \tag{6}$$

where *PEEQ*, *p*, and *q* are the equivalent plastic strain, the hydrostatic stress, and the von Mises stress, respectively. The equivalent plastic strain can be calculated using the following equation (Zhang et al., 2004):

$$PEEQ = \sqrt{\frac{2}{3}\varepsilon_{ij}\varepsilon_{ij}} \tag{7}$$

where ε_{ij} represents the plastic strain components.

The rupture index is used to evaluate and compare the fracture potential at different locations in a finite element model or a specific point in two different models. Research has shown that this criterion is highly accurate for evaluating fracture potential. A larger *RI* value indicates a greater potential for crack development and fracture (Rahnavard et al., 2015).

In order to assess the seismic performance of the DRBS connection, the maximum *RI* value at the beam-column interface was continuously evaluated during the loading. Since the rupture index is a comparative criterion for assessing crack development and fracture potential, *RI* values reaching the selected RI_{max} value cannot solely indicate weld fracture at the beam-column interface, and the *RI* values in the connection could be allowed to exceed the selected RI_{max} value. This violation of the selected upper limit was taken into account as a penalty function. For this purpose, a dynamic penalty function based on the multiplication method was chosen in such a way that if the maximum *RI* value exceeds the selected RI_{max} value, the function value becomes less than 1. This penalty function is multiplied by the area of each individual hysteresis loop at each time step of the analysis and dynamically reduces the objective function. The objective and penalty functions considered could thus be defined using the following equations:

$$\text{maximize } F = \Sigma \bar{E}(t) \tag{8}$$

$$\bar{E}(t) = E(t) \times P(t) \tag{9}$$

$$P(t) = \begin{cases} 1, & RI(t) \le RI_{max} \\ RI_{max}/RI(t), & RI(t) \ge RI_{max} \end{cases} \tag{10}$$

In Eq. (8), F is the objective function that is to be maximized in the optimization process, equal to the total area of the hysteresis loops with the penalty function applied ($\Sigma \bar{E}(t)$). For each cycle, $\bar{E}(t)$ is obtained by multiplying the penalty function ($P(t)$) by the area of the corresponding hysteresis loop ($E(t)$) as in Eq. (9). Furthermore, the maximum RI value at each time step of the analysis ($RI(t)$) is calculated using Eq. (6). If this value does not exceed the selected RI_{max} value, the penalty function will be equal to 1 as defined in Eq. (10); Otherwise, if $RI(t)$ exceeds the selected RI_{max}, the penalty function will be less than 1, hence reducing the calculated dissipated energy based on Eq. (9). In other words, by applying this penalty, the value of the objective function is reduced, which is contrary to the defined optimization goal. A higher $RI(t)$ value leads to a more significant decrease in the objective function value, and therefore a worse seismic performance from the connection.

2.3 Optimization Parameters

Based on Fig. 1, the cut profile in the DRBS connection involves the following six parameters:

- a_1: the distance between the column face and the start of the first reduced section.
- b_1: length of the first reduced section.
- c_1: depth of the first reduced section.
- a_2: the distance between the column face and the start of the second reduced section.
- b_2: length of the second reduced section.
- c_2: depth of the second reduced section.

The above parameters, also shown in Fig. 3, were used in the performance analysis and optimization of the DRBS connection in this research project. In the case of the RBS connection, which includes a single reduced section, the cut parameters include the single set a, b, and c.

2.4 CPSO Engine

In this research project, an optimization engine was developed based on the CPSO algorithm and the above-mentioned objective function in order to perform an automatic optimization process without human intervention. This CPSO engine, whose source was written as Octave commands, creates a link between this mathematic computation software and the finite element software used to analyze the connections considered. This engine starts by receiving information and parameters related to modeling each connection from the user and storing them. Next, it communicates with the finite element software and analyzes the connection under the specified loading after forming a model based on the data received. In the next step, the engine receives the analysis results from finite element software and updates the model after evaluating and altering the cut parameters using the CPSO algorithm. This process continues as a series of iterations until the optimization goal is satisfied and the optimum parameters are obtained. It should be noted that the values for cut parameters at the beginning of the process mentioned above are randomly chosen from their acceptable ranges. The simplified mechanism of the CPSO engine developed could be expressed as the flowchart presented in Fig. 4.

3 Finite Element Modelling

3.1 Modeling Method and Verification

Two element types of the continuum (solid) and shell families were selected for the finite element modeling done in this study. The continuum (solid) type selected was the C3D8R 8-noded reduced-integration brick element, with one integration point in its center. The shell type selected was the S4R 4-node reduced-integration shell element, also with one integration point. In case one of the dimensions of the model (its thickness) is much smaller than the other two dimensions and the stresses in the direction of the thickness of the model can be ignored, the shell element can be

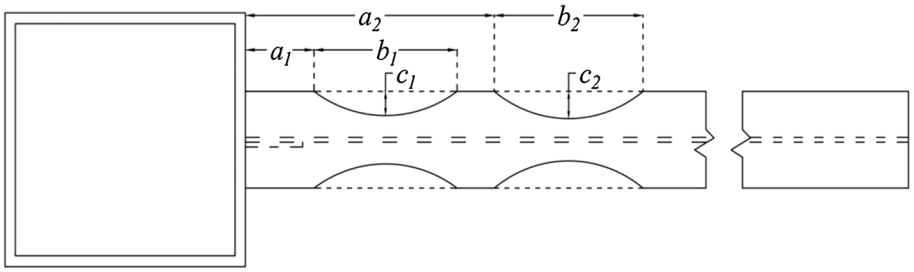

Fig. 3 Optimization parameters in the DRBS connection

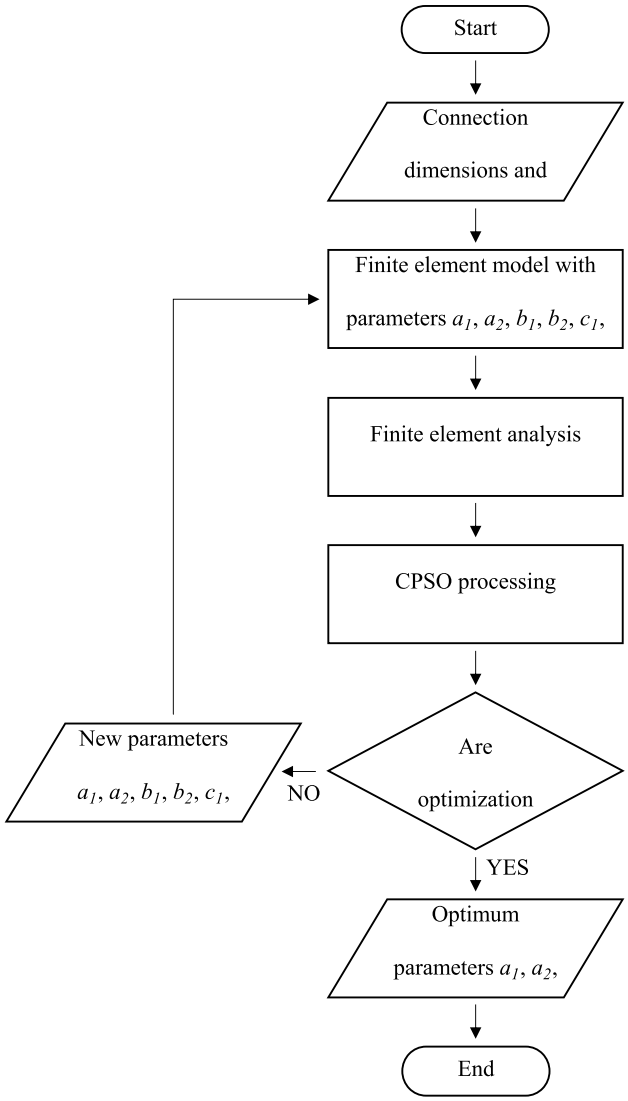

Fig. 4 Flowchart of the developed CPSO engine

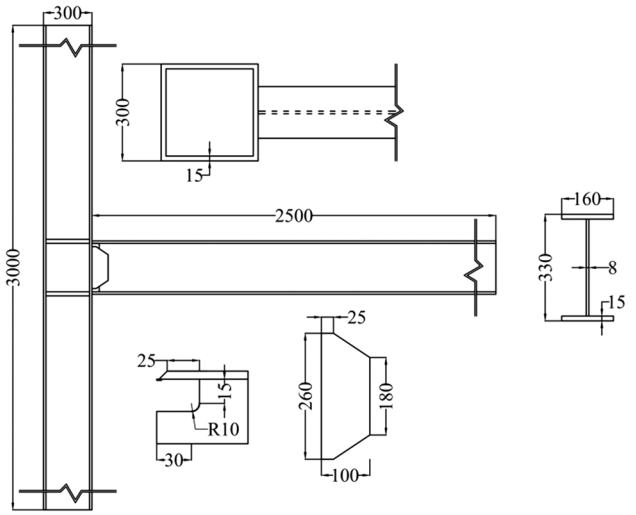

Fig. 5 Specimen DC-S tested by Nia et al. (2013) (dimensions in mm)

used for finite element modeling. The S4R element is suitable for modeling plastic and buckling behavior as well as large deformations and strains. Previous research, such as the paper by Foraboschi (2020), has also confirmed that this element's appropriacy for modeling steel members.

In order to ensure accurate modeling, a full-scale connection previously tested by Nia et al. (2013) was modeled as a verification specimen, and the finite element analysis results obtained were compared to the available experimental data. This specimen, named DC-S, was a welded unreinforced flange-welded web (WUF-W) moment connection between built-up I-beam and box-column structural elements. The I-beam in specimen DC-S had lateral bracing at a distance of 1.5 m from the column face.

Dimensions and details for specimen DC-S, including column and beam sections, shear plate, and weld access hole, are shown in Fig. 5. The loading protocol used in Nia et al.'s (2013) study for evaluating the cyclic behavior of specimen DC-S followed the recommendations of ANSI/AISC 341-16 (2016a), similar to those provided by FEMA 350 (2000).

The material used in the Nia et al.'s (2013) study was the ST-37-2 steel with a modulus of elasticity of 210 GPa and a Poisson's ratio of 0.3. In the present study, the combined hardening method, which involves four hardening parameters, was utilized to model the inelastic and nonlinear behavior of the steel used in the actual connection. Previous research (Collin et al., 2009) suggests that using a combination of isotropic and kinematic hardening models provides a better description of the cyclic behavior of the materials. In the combined hardening method, the parameters Q and B are used to model the isotropic hardening of the material.

Q shows the largest change in the size of the yield surface, and B shows the rate of change in the yield surface with the increase of plastic strain. Furthermore, the parameters C and γ are used to model the kinematic hardening of the material. C is the modulus of initial kinematic hardening, and the dimensionless coefficient γ represents the reduction rate of kinematic hardening with the increase in plastic deformation. In a tensile test, where only the tensile stress is present, the following equation could be established between the four aforementioned parameters based on the combined hardening method (Collin et al., 2009):

$$\sigma = \sigma_y + Q\left(1 - \exp\left(-B\varepsilon_p\right)\right) + \frac{C}{\gamma}\left(1 - \exp\left(-\gamma\varepsilon_p\right)\right) \tag{11}$$

where σ, σ_y, and ε_p represent the stress, yield stress, and plastic strain, respectively.

The appropriate values for the four combined hardening parameters used in the finite element software were determined through a trial-and-error procedure aimed at satisfying the following criteria:

(1) Compliance between the stress-plastic strain curves obtained from Eq. (11) and the tensile test results provided in Nia et al.'s (2013) study.
(2) Compliance between the hysteresis loops of the finite element model and the specimen tested in Nia et al.'s (2013) study.
(3) Compliance between the behavior of the finite element model and the specimen tested in Nia et al.'s (2013) study.

The appropriate values of the hardening parameters used in finite element modeling, obtained after about 50 trial-and-error runs with different values, are presented in Table 1.

Figure 6 shows the stress-plastic strain curves of the materials assigned to different members of the finite element model, plotted using the obtained material parameters presented in Table 1. The yield and ultimate stress values in these curves perfectly matched the original test data of Nia et al.'s (2013) study.

Geometric nonlinearity is also regarded as another source of nonlinear behavior that should be taken into account during a finite element analysis. This phenomenon should be especially considered when large deformations and rotations or structural instability such as buckling occurs. In the present study, the nonlinear factor related to the connection geometry was considered in the analyses conducted by activating the NLGEOM (Nonlinear Geometry) option in the ABAQUS finite element software.

The specimen DC-S introduced above was modeled in the finite element software using the shell element introduced above. A second model, generated with the introduced continuum element, was also considered to ensure that the modeling results are accurate.

Figure 7 shows the model created using the shell element along with the boundary conditions, the applied loading, and the resulting finite element mesh. The model was generated using a variable mesh size of between 2 and 6 cm, with the smaller meshing used for the panel zone and the plastic hinge areas to increase accuracy in capturing local behaviors. In addition, the hinge and roller supports of the specimen were modeled as displacement constraints in specific directions.

Figures 8 and 9 present the comparison of the hysteresis loops of specimen DC-S tested by Nia et al. (2013) and those of the models created using shell and continuum elements and the assumed material parameters. As can be seen, there was a very good similarity between the behaviors of the tested specimen and each of its finite element models. Moreover, based on Figs. 10 and 11, it can be seen that the von Mises stress distribution, deformations, and local buckling behavior of specimen DC-S tested by Nia et al. (2013) and those of the models created using shell and continuum elements very similar.

The advantage of shell elements over continuum elements is that they allow for faster modeling and shorter computation times with less computer memory and storage capacity. According to the results, the shell element simulated the behavior of specimen DC-S just as well as the continuum element utilized. Hence, considering the aforementioned advantages of shell elements and the large number of analyses required, the shell element introduced was chosen to model the connections in this study.

Table 1 The material parameters used in the finite element modeling

Member	γ	C (GPa)	B	Q (MPa)	σ_y(MPa)
Beam flange plate	24.0	2.5	8	49.2	252.0
Beam web plate and shear plate	24.8	2.5	8	43.7	351.0
Column plate	28.5	2.5	4	37.1	252.9
Continuity plate	46.0	2.5	4	23.0	252.5

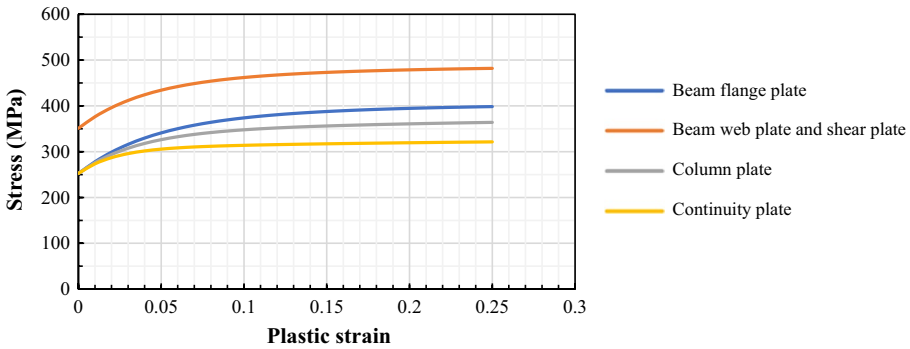

Fig. 6 The stress-plastic strain curve used in the finite element modeling

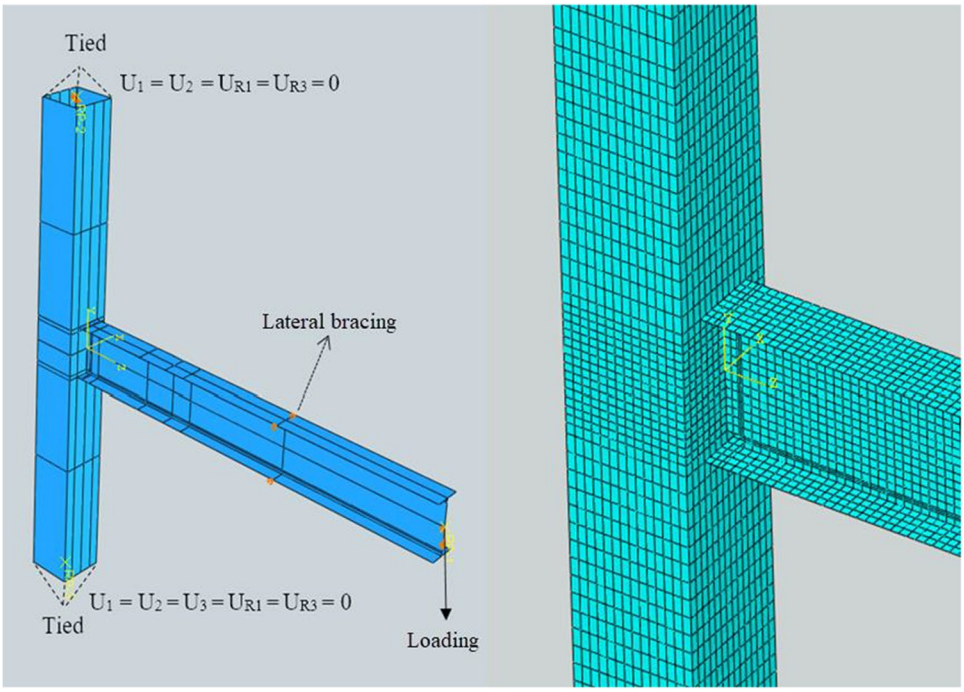

Fig. 7 The model of the specimen DC-S generated using the shell element

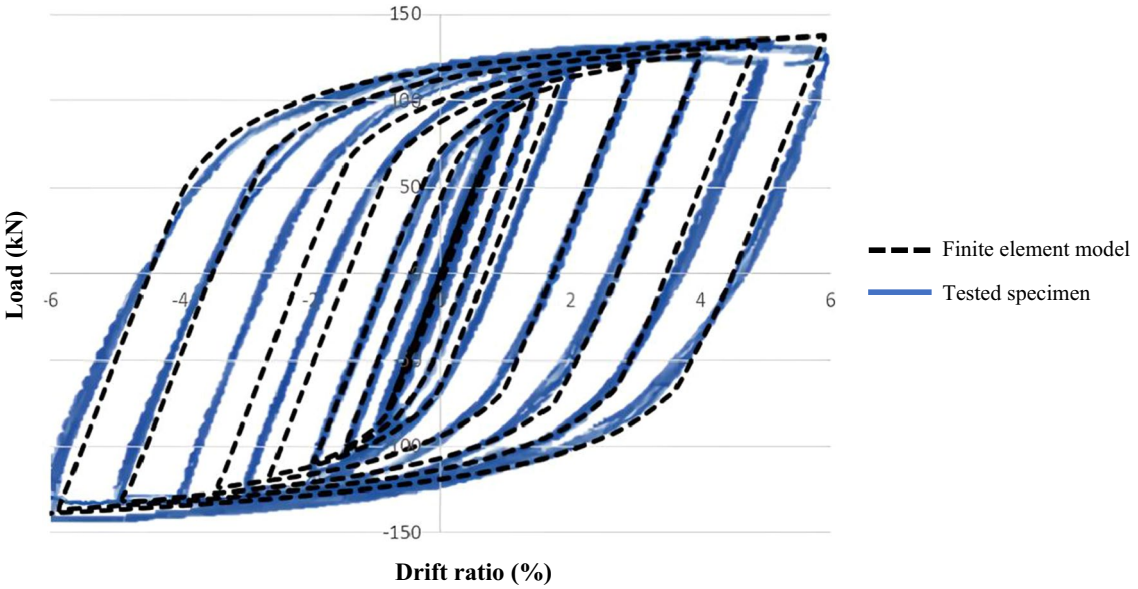

Fig. 8 Hysteresis loops of specimen DC-S tested by Nia et al. (2013) and the model created using the continuum element

3.2 Modeled Connections

In this study, three DRBS I-beam to box-column connections were modeled and optimized for the different RI_{max} cases using the CPSO engine developed. The dimensions and design specifications of the beam and column sections in these connections, obtained from Nia et al.'s (2013) study, were such that they represented small, medium, and large DRBS connections and thus are respectively referred to as connections D-S, D-M, and D-L throughout this text. This classification made it possible to determine the effect of the beam and column section size on the optimum shape and seismic performance of the DRBS connection.

The optimization procedure also included a standard RBS connection, which was modeled and optimized to confirm the accuracy of the developed CPSO engine. The dimensions

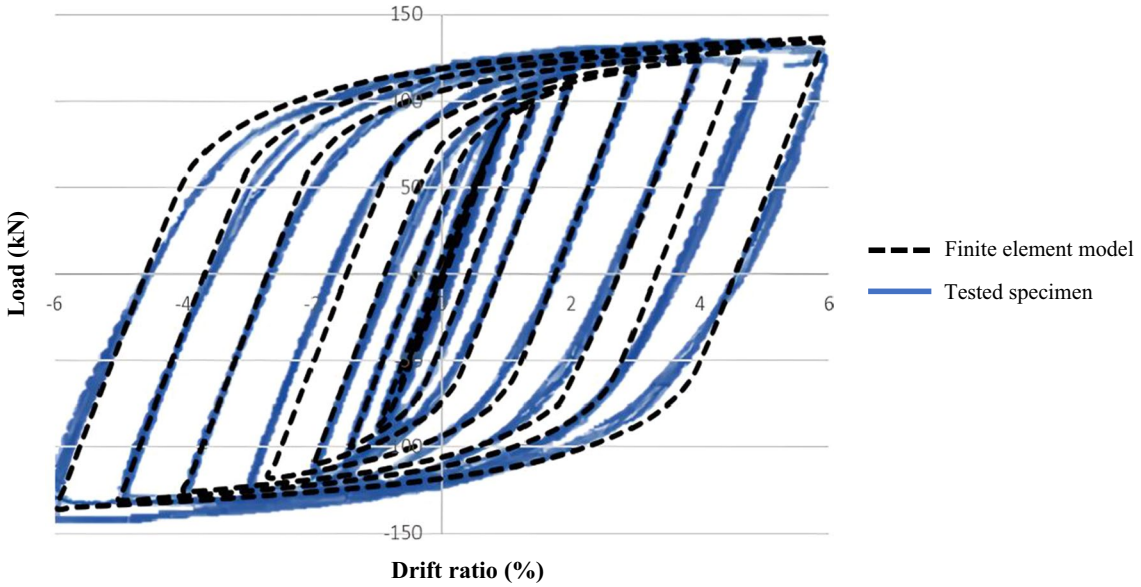

Fig. 9 Hysteresis loops of specimen DC-S tested by Nia et al. (2013) and the model created using the shell element

and other design specifications of this connection, which is referred to as connection R-S throughout this text, were identical to those of connection D-S introduced above so that the results obtained could be used for comparing the RBS and DRBS connections.

Tables 2, 3, 4 present the design specifications of the beam, column, and panel zone in the modeled connections. According to these tables, it is clear that the specifications met the strong column/weak beam design criteria, which is one of the critical controls in the design of connections in special moment frames. Furthermore, the shear strength of all the panel zones was higher than the shear strength demand. The panel zone could thus be considered to be strong in all the connections considered. It should be noted that according to seismic regulations, weak panel zones increase the probability of groove weld fractures in connections. The geometry of the weld access hole in all of the modeled connections followed the provisions of both ANSI/AISC 360-16 (2016c) and ANSI/AWS D1.8/D1.8M:2016 (2016).

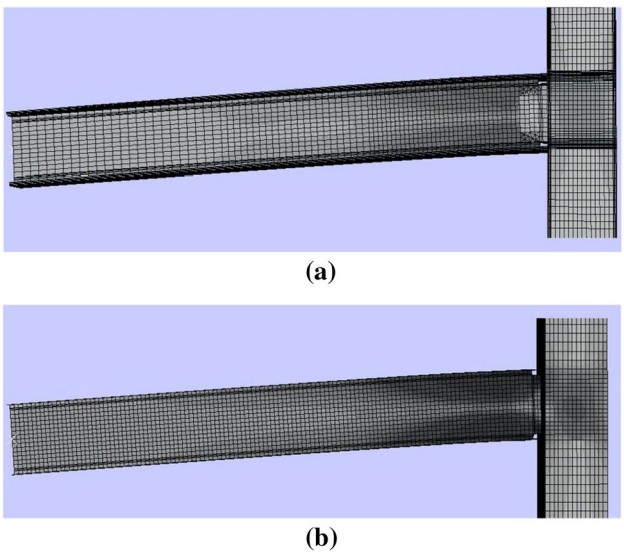

Fig. 10 von Mises stress distribution in the generated models at 6% drift ratio: **a** model with continuum element, **b** model with shell element

3.3 Loading Protocol

Cyclic loading was applied to the modeled connections in the form of displacement at the free end of the beam. Figure 12 shows the cyclic loading protocol used in the finite element software, which was based on the provisions of ANSI/AISC 341-16 (2016a) and FEMA 350 (2000).

4 Optimization Results

4.1 Connection R-S

In order to confirm the accuracy of the developed CPSO engine, it was first tested on the RBS connection R-S introduced in Sect. 3.2. The resulting optimum cut parameters followed a consistent and acceptable trend, and hence it was concluded that the CPSO engine could also be suitable for optimizing the DRBS connections considered. This section provides a summary of the optimization procedure for connection R-S and the obtained results.

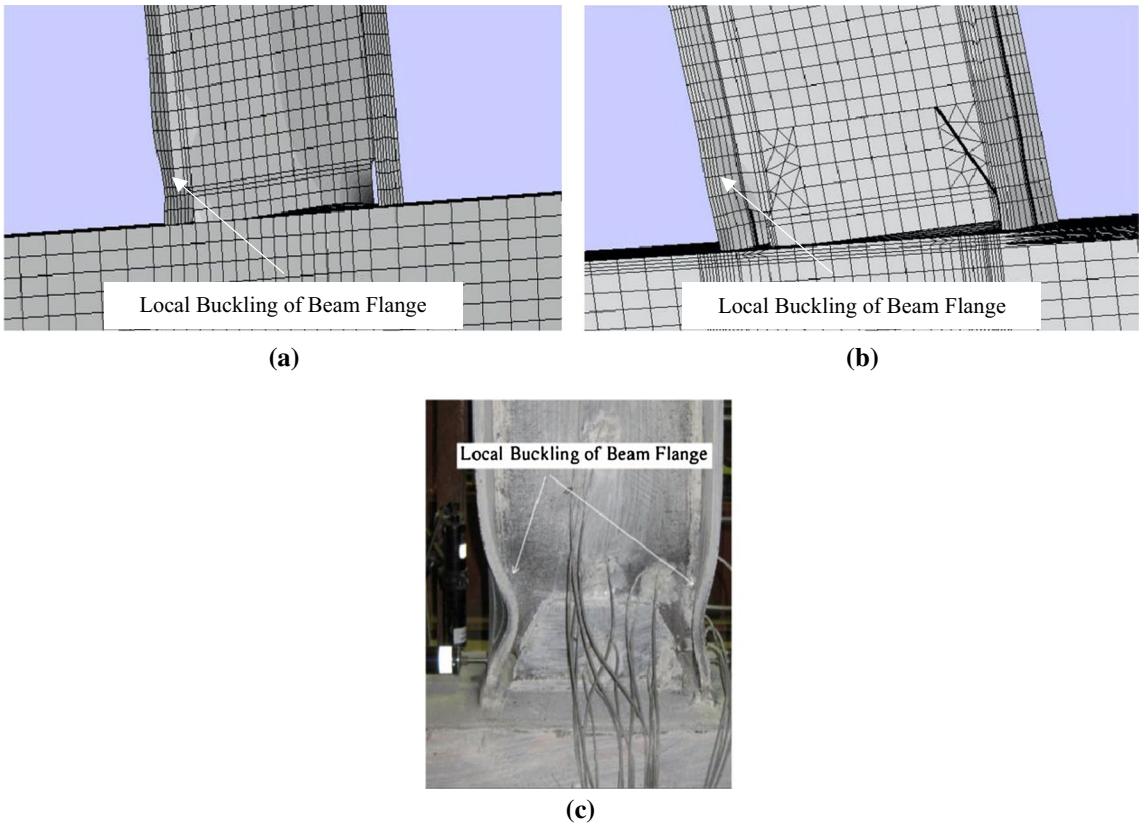

Fig. 11 Similarity of the deformations and failure modes of the generated models with those of specimen DC-S tested by Nia et al. (2013) at 6% drift ratio: **a** model with shell elements, **b** model with continuum element, **c** specimen DC-S tested by Nia et al. (2013)

Table 2 Specifications of the modeled connections

Connection	Type	b_{bf} (cm)	t_f (cm)	H_{beam} (cm)	t_w (cm)	b_c (cm)	t_c (cm)	t_{cp} (cm)
R-S	RBS	16	1.5	33	0.8	30	1.5	2.5
D-S	DRBS	16	1.5	33	0.8	30	1.5	2.5
D-M	DRBS	24	1.5	33	0.8	40	2.0	2.5
D-L	DRBS	24	2.0	38	0.8	50	2.5	2.5

Table 3 Design specifications of the beam and column sections in the modeled connections

Connection	Z_{pb} (cm^3)	M_{pr} (kN m)	V_h (kN)	Z_{pc} (cm^3)	ΣM_{pc} (kN m)	ΣM_{pb} (kN m)	$\Sigma M_{pc}/\Sigma M_{pb}$
R-S	936	360	150	1800	780	760	1.03
D-S	936	360	150	1800	780	760	1.03
D-M	1314	490	200	4300	1600	1200	1.34
D-L	1596	780	310	8500	3000	3400	1.74

$M_{pr} = C_{pr}\, R_y\, F_y\, Z_{pb}$, $V_h = (2M_{pr})/L$, $\Sigma M_{pc} = \Sigma\, Z_{pc} F_y$, $\Sigma M_{pb} = \Sigma(M_{pr} + V_h \times b_c/2)$

In the first iteration of the CPSO algorithm, the values for the optimization parameters in connection R-S, namely a, b, and c, were randomly chosen from their acceptable ranges. The population of particles was chosen to be ten times the number of optimization parameters, equal to 30 particles. Therefore, 30 finite element analyses were conducted in each iteration of the optimization algorithm so that the objective function was calculated for all the particles involved. The new values for the cut parameters for connection R-S were selected from the following limits enforced during the optimization process:

Table 4 Design specifications of the shear plate in the modeled connections

Connection	P_c (kN)	R_n (kN)	$(M_{pl}/H_{beam})/\varphi R_n \leq 1$	V_n (kN)	V_h (kN)	$(V_h)/(\varphi V_n) \leq 1$
R-S	460	140	0.9	48	150	760
D-S	460	140	0.9	48	150	760
D-M	770	240	0.7	56	200	1200
D-L	1200	390	0.6	53	310	3400

$R_n = 0.6\, F_y\, d_c\, t_p, V_n = 0.6\, F_y\, A_{web}\, C_v$

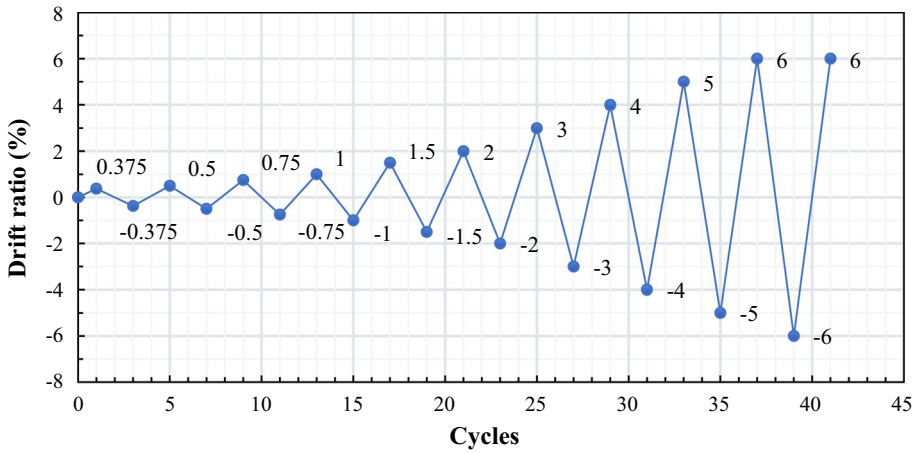

Fig. 12 The cyclic loading protocol used in the optimization procedure (ANSI/AISC 341-16, 2016a; FEMA 350, 2000)

$$\left\{\begin{array}{c} 0.50b_{bf} \leq a \leq b_{bf} \\ 0.65H_{beam} \leq b \leq H_{beam} \\ 0.05b_{bf} \leq c \leq 0.25b_{bf} \end{array}\right\} \quad (12)$$

where b_{bf} and H_{beam} are the beam flange width and beam depth, respectively. According to ANSI/AISC 358-16 (2016b), the values of a and c are proportional to the beam flange width, and the value of b is proportional to the beam depth. To assess the cut parameters more accurately, their acceptable ranges were increased compared to those defined by ANSI/AISC 358-16 (2016b). The upper limit for the reduced section depth c was set equal to the one specified by ANSI/AISC 358-16 (2016b) to keep the reduction in the cross-sectional area of each beam flange below 50%.

Before selecting the RI_{max} values, it was necessary to calculate the maximum rupture index in an equivalent non-RBS connection with the same design specifications as those introduced for connection R-S. This parameter, termed RI_{final}, was calculated to be equal to 1.57 in a connection equivalent to connection R-S. The desired RI_{max} values could thus be selected as specific percentages of RI_{final}. The optimization procedure for connection R-S was performed with nine different cases of RI_{max} values. The RI_{max} and the corresponding RI_{max}/RI_{final} cases considered in the optimization of connection R-S are presented in Table 5.

Table 5 RI_{max} and corresponding RI_{max}/RI_{final} cases used in the optimization of connection R-S

Case	RI_{max}	RI_{max}/RI_{final}
1	0.1	0.06
2	0.3	0.19
3	0.4	0.25
4	0.7	0.45
5	0.9	0.57
6	1.0	0.64
7	1.1	0.70
8	1.4	0.89
9	1.6	1.02

About 5400 finite element analyses were conducted by the CPSO engine during the optimization process of connection R-S. The resulting normalized optimum cut parameters for the RI_{max} cases considered are shown in Fig. 13. The values in this table are dimensionless and normalized with respect to the beam flange width (b_{bf}), for a and c, and beam depth (H_{beam}) for b. For all RI_{max} cases considered, the results indicated a convergence in the objective function values, and the algorithm successfully found the optimal answer in the problem space. The horizontal lines in Fig. 13 indicate the limits defined by ANSI/AISC 358-16 (2016b).

The results showed that the optimum value for the parameter a increased with the increase of RI_{max}. More precisely, based on the pattern observed, it can be said that if no upper

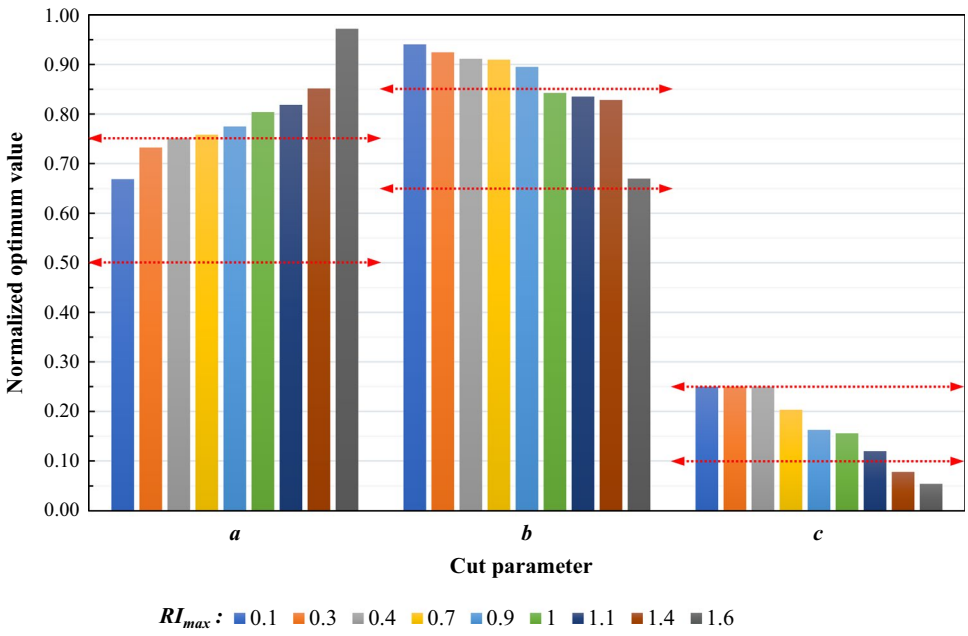

Fig. 13 Normalized optimum cut parameters obtained for connection R-S

limit is set for the *RI* value, the optimum shape will tend towards the simple non-RBS connection, so that the total area of the hysteresis loops and hence the objective function value are maximized through the increased moment at the column face. Nevertheless, the increase in the moment at the column face increases the stress, strain, and the resulting *RI* values at the beam-column interface, and therefore reduces the efficiency of the connection. In other words, at a particular displacement applied, the moment at the column face in a simple connection without a reduced section is higher than that in an RBS connection, which results in increased hysteresis loop area because of increased loop height. Thus, the increase in RI_{max} leads to increased optimum *a* value, allowing for increased moment at the column face. Based on Fig. 13, it can be seen that for $RI_{max} < 0.9$, the optimum values obtained for the parameter *a* were approximately within the limits defined by ANSI/AISC 358-16 (2016b). In contrast, for $RI_{max} < 0.9$, the optimum *a* value tended towards values higher than the upper limit defined by ANSI/AISC 358-16 (2016b).

The trend in the results obtained for the parameter *b* indicates that the optimum length of the reduced section increased with the decrease in RI_{max}. The increase in *b* allows for the decrease in *RI* values demanded by a low RI_{max}. On the other hand, with the increase in RI_{max}, the demand to limit the *RI* values is reduced. A lower *b* value leads to a smaller reduced section and greater moment at the column face, which results in an increased hysteresis loop area. Therefore, the optimum value for the parameter *b* decreased when a higher RI_{max} was selected. For $0.1 \leq RI_{max} \leq 0.4$, the optimum values obtained for *b* were approximately 7% to 10% higher than the upper limit defined by ANSI/AISC 358-16 (2016b). In contrast, for $RI_{max} > 0.7$, the resulting optimum values of *b* were lower and approximately within the limits defined by ANSI/AISC 358-16 (2016b). It can be concluded that with the decrease of RI_{max} the optimum *b* value tends towards increasing to values higher than the limits defined by ANSI/AISC 358-16 (2016b). Increased *b* results in longer and hence larger cuts in the beam flanges, which in turn further decrease the *RI* values at the beam-column interface.

The parameter *c* followed a similar trend as that of *b* when RI_{max} increased. In other words, the optimum value of *c* also decreased with the increase of RI_{max}. An upper limit equal to 25% of the beam flange width, the same as that defined by ANSI/AISC 358-16 (2016b), was considered for *c* to prevent an excessive reduction in the flange cross-sectional area. According to the results, for $RI_{max} \leq 0.4$, the optimum *c* value remained equal to this upper limit. However, the optimum *c* value decreased with the further increase of RI_{max}. Hence, it can be concluded that the optimum shape tends towards reduced sections with less depth when a higher RI_{max} is desired. If no upper limit is considered for the parameter *c*, the optimum value for $RI_{max} \leq 0.4$ is likely to become higher than the upper limit defined by ANSI/AISC 358-16 (2016b), similar to the results for *b*. That way, the reduction in the cross-sectional area of each beam flange exceeds 50%, which is not accepted according to ANSI/AISC 358-16 (2016b). The increase in *c* results in less moment at the column face. Subsequently, due to the decrease in stress, strain, and rupture index at the column beam-column interface, the penalty function value also decreases, and therefore, the objective function reaches a higher value. The results obtained suggest that the optimum

reduced section has smaller cuts and a greater distance from the column face when a higher RI_{max} is desired.

Overall, it can be concluded that if no maximum limit for the rupture index value at the beam-column interface is considered, the optimum shape of the RBS connection will tend towards the simple non-RBS connection without a reduced section, which allows for the maximum possible total area of the hysteresis loops.

4.2 Connection D-S

The first DRBS connection optimized was connection D-S introduced in Sect. 3.2. The dimensions and other design specifications of connection D-S were identical to connection R-S optimized earlier so that the results obtained for these two connections could be used for comparing RBS and DRBS connections.

In the first iteration of the CPSO algorithm, the values for the six cut parameters involved were randomly chosen from their acceptable ranges. The population of particles was chosen to be ten times the number of optimization parameters, equal to 60 particles. Therefore, 60 finite element analyses were conducted in each iteration of the CPSO algorithm so that the objective function was calculated for all particles involved. The CPSO algorithm ran for a total of 25 iterations for each RI_{max} case considered. The results for all RI_{max} cases indicated a convergence in the objective function value, and hence the successful calculation of the optimal answer in each problem space.

The new values for the cut parameters were selected from the following limits enforced during the optimization process:

$$\left\{\begin{array}{c} 0.50b_{bf} \le a_1 \le b_{bf} \\ 0.65H_{beam} \le b_1 \le H_{beam} \\ 0.05b_{bf} \le c_1 \le 0.35b_{bf} \\ 0.50\left(b_{bf}+H_{beam}\right) \le a_2 \le 3.00\left(b_{bf}+H_{beam}\right) \\ 0.20H_{beam} \le b_2 \le H_{beam} \\ 0.05b_{bf} \le c_2 \le 0.40b_{bf} \end{array}\right\} \quad (13)$$

The cut parameters of both reduced sections were set to be proportional to the beam flange width for a and c, and the beam depth for b, similar to the ANSI/AISC 358-16 (2016b) specifications for the RBS connection. Considering the novelty of the DRBS connection and lack of sufficient information about this design, a wide range of acceptable values were considered to conduct a more comprehensive study and assess all possible values for the design parameters involved. It should be noted that the upper limit defined by ANSI/AISC 358-16 (2016b) for the parameter c in the RBS connection, equivalent to a maximum 50% reduction in the beam flange cross-sectional area, was not considered in the optimization of connection D-S. Thus, a broader problem space was defined, allowing for a more extensive investigation of the behavior of the DRBS connection.

Table 6 RI_{max} and corresponding RI_{max}/RI_{final} cases used in the optimization procedure of connection D-S

Case	RI_{max}	RI_{max}/RI_{final}
1	0.1	0.06
2	0.3	0.19
3	0.4	0.25
4	0.7	0.45
5	0.9	0.57
6	1.0	0.64
7	1.1	0.70
8	1.4	0.89

The optimization of connection D-S was done with the RI_{max} and the corresponding RI_{max}/RI_{final} cases presented in Table 6, similar to those considered for connection R-S. The following sections present the optimization results obtained for connection D-S and compare the DRBS and RBS connections in different aspects.

4.2.1 Optimum Parameters

The normalized optimum values of the six cut parameters obtained for the RI_{max} cases considered are presented in Fig. 14. The CPSO engine performed about 12,000 finite element analyses with different cut parameters to find these values. The horizontal lines drawn for the parameters of the first reduced section indicate the limits defined by ANSI/AISC 358-16 (2016b) for the cut parameters in the RBS connection. For a better interpretation of the results for connection D-S, the optimum shapes obtained for the RI_{max} cases considered are also schematically illustrated in Fig. 15.

According to Fig. 15, for $RI_{max} \le 0.7$, equal to up to 45% of RI_{final}, the optimum shape tended towards the DRBS connection. For $RI_{max} \ge 0.7$, the two adjacent reduced sections overlapped, and the optimum shape became similar to the RBS connection. For RI_{max} values close to RI_{final}, the flange cuts became smaller and almost non-existent. Therefore, it can be concluded that the DRBS connection is not the optimum shape for $RI_{max} \ge 0.7$. More precisely, for such RI_{max} values, the optimum shape is highly similar to the RBS connection.

Based on the results in Fig. 14, it is clear that for $RI_{max} \le 0.7$, the optimum values obtained for the parameter a_1 were within limits defined by ANSI/AISC 358-16 (2016b). The optimum a_1 value increased as the desired RI_{max} increased to up to 0.9. The optimum a_1 value followed a decreasing trend with further increase in RI_{max} except for $RI_{max} = 1.4$, where it increased towards the upper limit defined by Eq. (13).

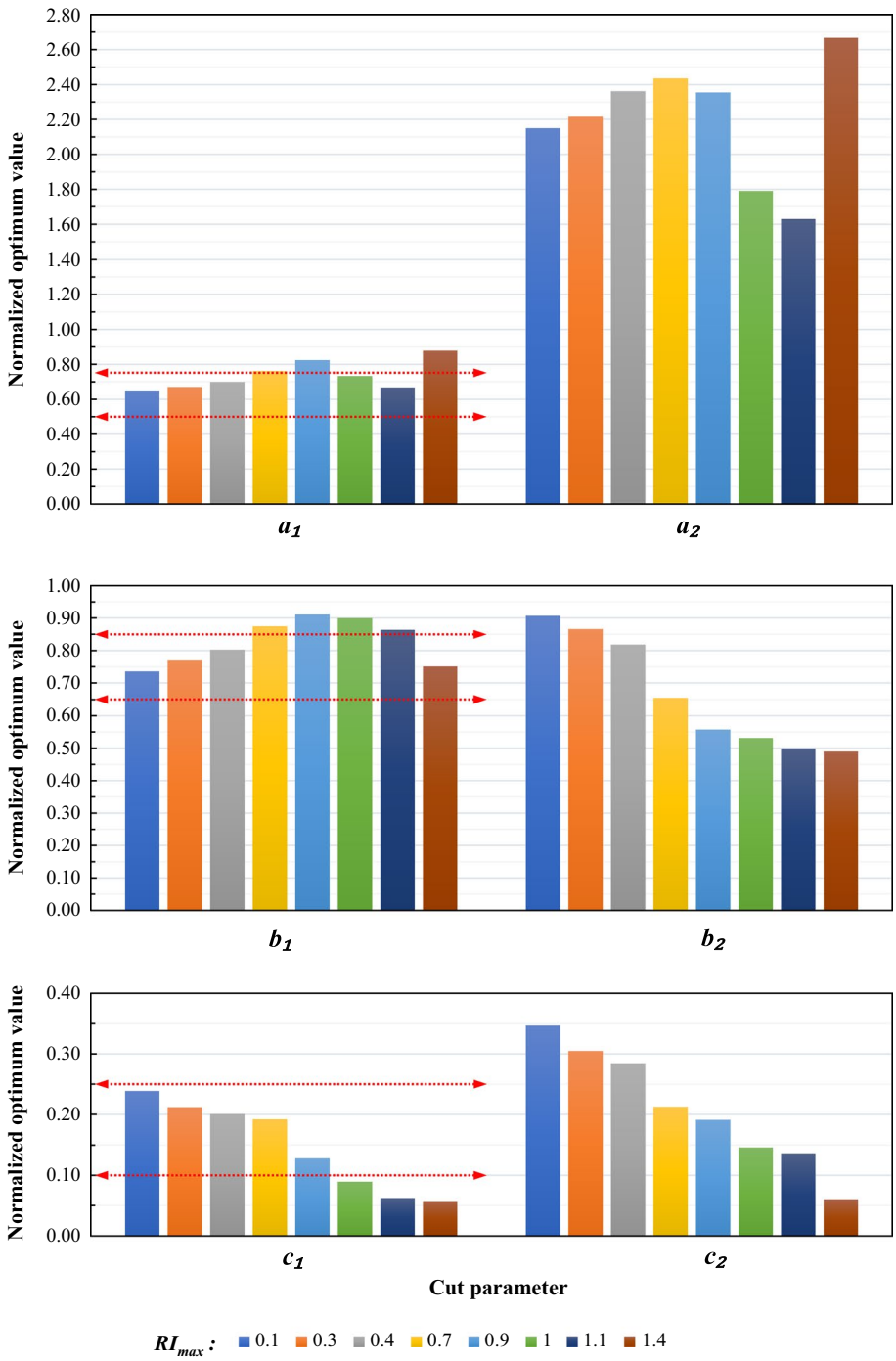

Fig. 14 Normalized optimum cut parameters for connection D-S

The parameter b_1 followed a trend roughly similar to that of a_1 as RI_{max} increased. In other words, the optimum b_1 value increased as RI_{max} increased to up to 0.9, and then it had a decreasing pattern with further increase in RI_{max}. For $RI_{max} \leq 0.7$, the optimum b_1 values obtained were within the limits defined by ANSI/AISC 358-16 (2016b). Such results are in contrast to those obtained for the parameter b in connection R-S, where the optimum values were higher for lower RI_{max} values and exceeded the upper limit defined by ANSI/AISC 358-16 (2016b) for $RI_{max} \leq 0.7$.

Based on the trends observed for the parameters a_1 and b_1 as well as the schematic illustrations of the optimum shapes, it can be concluded that the selected RI_{max} value has a significant effect on the optimum shape of the reduced sections in the DRBS connection. This matter is further discussed in the following.

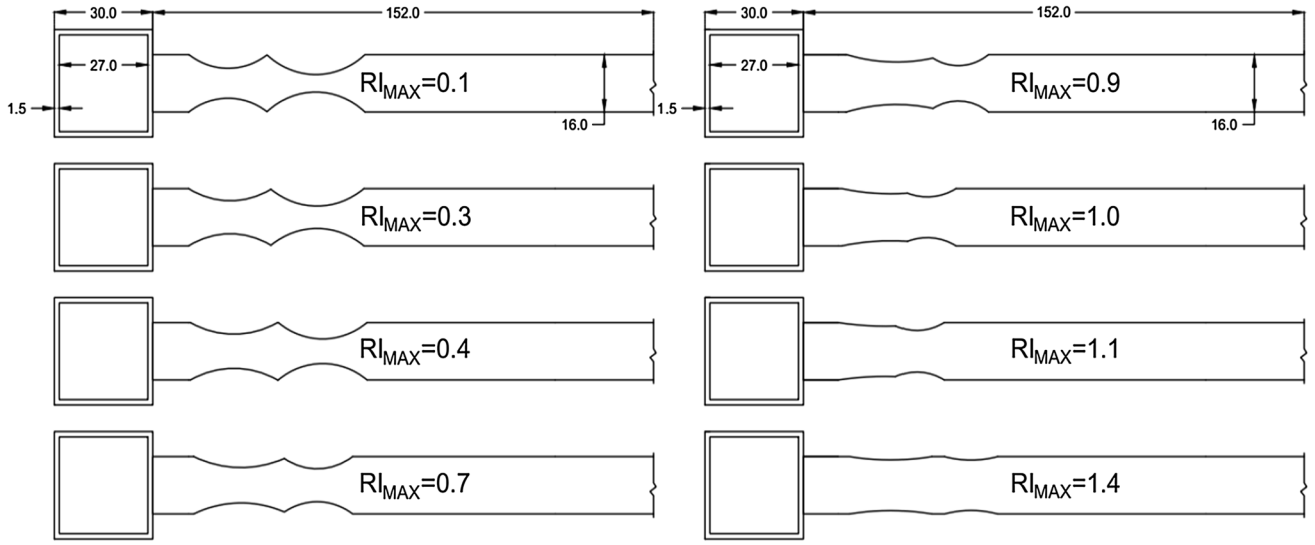

Fig. 15 Optimum shapes of connection D-S obtained for different RI_{max} cases (dimensions in cm)

Table 7 Optimum distance between the two reduced sections in connection D-S obtained for different RI_{max} cases

RI_{max}	d (cm)
0.1	−0.2
0.3	−0.6
0.4	0.1
0.7	−2.1
0.9	−5.6
1	−12.8
1.1	−13.0
1.4	3.9

The optimum value for the depth of the first reduced section decreased with the increase of RI_{max}. For $0.1 \leq RI_{max} \leq 0.9$, the optimum c_1 values obtained were between the limits defined by ANSI/AISC 358-16 (2016b). Such results are in contrast to those obtained for the parameter c in connection R-S, which suggests that this parameter is likely to reach values as high as 30% of the beam flange width resulting in an excessive reduction in the beam flange cross-sectional area if no upper limit is enforced.

One of the most important design parameters in the DRBS connection is the distance between the column face and the start of the second reduced section, i.e. a_2. The optimum values for the distance between the two reduced sections ($d = a_2 - (a_1 + b_1)$), dependent on a_2 are given in Table 7. In the case of overlap between the two reduced sections, the resulting value of d becomes negative. Thus, the negative values in Table 7 indicate the amount of overlap between the reduced sections in each optimum shape obtained.

According to Table 7 and Fig. 15, there was almost no overlap between the two reduced sections in the optimum shape for $RI_{max} \leq 0.4$. More precisely, in the optimum shapes obtained for such RI_{max} cases, the second reduced section started approximately at the same point where the first reduced section ended. In other words, the optimum a_2 value was approximately equal to the sum of optimum a_1 and b_1 values. Nevertheless, for $RI_{max} \geq 0.7$, the two reduced sections overlapped as a result of the decrease in the a_2 value, and hence the optimum shape tended towards the RBS connection as RI_{max} increased. For $RI_{max} = 1.4$, the two reduced sections in the resulting optimum shape were at some distance apart and did not overlap. Thus, it seems that for RI_{max} values close to RI_{final}, the flange cuts in the optimum shape tend to get smaller and farther from the column face. Such a shape decreases the limiting effect of the reduced sections on the moment transferred to the column face. Therefore, as a result of the increased moment at the column face, the objective function is further maximized.

The trend followed by the parameter b_2 was the same as that of b in connection R-S. In other words, the length of the second reduced section increased as RI_{max} decreased. For $RI_{max} \leq 0.4$, the optimum value obtained for b_2 was higher than that of b_1. More precisely, the optimum b_2 for such RI_{max} values ranged between 80 and 90% of the beam depth, about 5% higher than the upper limit defined by ANSI/AISC 358-16 (2016b) for the length of the reduced section in the RBS connection.

The optimum value of the parameter c_2 in connection D-S increased with the decrease of RI_{max}. Moreover, the optimum value of c_2 was higher than that of c_1 for all RI_{max} cases considered. This result is due to the fact that the bending moment induced in the second reduced section is lower than that in the first one. Therefore, the depth of the second reduced section has to be more than that of the first one to

allow for the simultaneous plasticization of these sections. For RI_{max} values equal to 0.1, 0.3, and 0.4, the decrease in the cross-sectional area of each beam flange at the first reduced section was equal to 69%, 61%, and 57%, respectively. As for the second reduced section, the decrease in the cross-sectional area of each beam flange for the same set of RI_{max} values were 48%, 42%, and 40%, respectively.

As seen in Fig. 15, the flange cuts in the optimum shape tended towards getting smaller and farther from the column face as RI_{max} reached high values. Overall, as in the case of the RBS connection, it can be concluded that if no maximum limit is set for the rupture index value at the beam-column interface, the optimum shape of the DRBS connection will tend towards the non-RBS connection. Such a design lessens the limiting effect of reduced sections on the moment transferred to the column face. In other words, it increases the amount of moment transferred, leading to the increase in the height of the hysteresis loops. Hence, the objective function is maximized.

4.2.2 Objective Function, RI, and PEEQ Values

The first part of Table 8 presents the percentage decrease in the optimum objective function values obtained for connections R-S and D-S after applying the penalty function in each RI_{max} case considered. According to this table, for $0.1 \le RI_{max} \le 0.4$, the decrease in the optimum objective function value calculated for connection D-S was significantly lower than that obtained for connection R-S. The second part of Table 8 presents the percentage difference in the optimum objective function values obtained for connections R-S and D-S. Based on the results, it is clear that for $0.1 \le RI_{max} \le 0.4$, the DRBS connection resulted in an increased optimum objective function value compared to the RBS connection. Nonetheless, for $RI_{max} \ge 0.7$, the DRBS connection did not lead to any improvement in the optimum objective function value.

Based on the results for connections R-S and D-S, the maximum *RI* and *PEEQ* values at the beam-column interface in the optimum shapes significantly decreased with the decrease in RI_{max}. Lower maximum *RI* and *PEEQ* values at the beam-column interface indicate lower brittle failure probability and better connection performance. Therefore, such improvements justify the lower objective function values in RBS and DRBS connections compared to that in the simple non-RBS connection.

Furthermore, the results obtained showed that for $0.1 \le RI_{max} \le 0.4$ the optimum shape of connection D-S had a better performance compared to that of connection R-S. More precisely, in almost all of the RI_{max} cases, the maximum *RI* and *PEEQ* values at the beam-column interface in the optimum shape of connection D-S were lower than those in that of connection R-S. Table 9 presents the percentage difference in the maximum *RI* and *PEEQ* values at the beam-column interface in the optimum shapes of connection R-S and D-S. According to this table, it is clear that for $0.1 \le RI_{max} \le 0.4$, the maximum *RI* and *PEEQ* values calculated in the optimum shape of connection D-S were significantly lower than those in that of connection R-S. Hence, the DRBS connection resulted in a considerably improved seismic behavior in this RI_{max} range. However, the results show no significant change in the maximum *RI* and *PEEQ* values for $RI_{max} \ge 0.7$. In fact, in one case ($RI_{max} = 1.0$), the optimum shape of connection D-S even had higher maximum *RI* and *PEEQ* values than that of connection R-S.

Overall, the results discussed above suggest that using the DRBS connection leads to better seismic behavior compared to the RBS connection for $RI_{max} \le 0.4$. However, for $0.4 < RI_{max} \le 0.9$, the optimum connection shape appears to be the conventional RBS connection. The results obtained also indicate that the optimum connection shape tends towards the simple non-RBS connection for $RI_{max} > 0.9$. Hence, the best design varies between the following three connections depending on the RI_{max} value desired:

Table 8 Comparison of the optimum objective function values in connections R-S and D-S

RI_{max}	Decrese after penalty function application (%)		D-S versus R-S (%)
	R-S	D-S	
0.1	64.6	43.4	38.5
0.3	23.1	7.4	9.8
0.4	10.2	2.3	5.0
0.7	3.1	1.2	−0.3
0.9	3.8	0.3	0.6
1.0	1.0	2.7	−0.1
1.1	1.2	0.9	1.5
1.4	0.0	0.0	−1.9

Table 9 Difference in the maximum *RI* and *PEEQ* values; D-S versus R-S (%)

RI_{max}	*RI*	*PEEQ*
0.1	−50.8	−55.2
0.3	−36.2	−32.9
0.4	−28.9	−32.7
0.7	−9.5	−7.9
0.9	−14.5	−14.7
1.0	6.5	7.0
1.1	−2.3	−1.6
1.4	−3.1	−3.1

- The DRBS connection for strictly low RI_{max} values (less than 25% of RI_{final}).
- The RBS connection for moderate RI_{max} values (between 25 and 60% of RI_{final}).
- The simple non-RBS connection for high RI_{max} values (more than 60% of RI_{final}).

4.2.3 Von Mises Stress and PEEQ Distribution

The von Mises stress and *PEEQ* distributions in the optimum shapes obtained for connection D-S showed that for $0.1 \leq RI_{max} \leq 0.4$, utilizing the DRBS connection shifts the maximum stress location away from the beam-column interface and to the two reduced sections. Figure 16 shows von Mises stress and *PEEQ* index distributions in the optimum shape of connection D-S for $RI_{max} = 0.3$ as an example. Based on the von Mises stress distribution obtained, it can be concluded that for $0.1 \leq RI_{max} \leq 0.4$, the DRBS connection is capable of shifting the plastic hinge location away from the beam-column interface through weakening the beam section, similar to the RBS connection. The *PEEQ* distribution in the optimum shapes of connection D-S obtained for the RI_{max} range mentioned above also indicated that the maximum value of this index occurred at the two reduced sections. Shifting of the stress concentration away from the beam-column interface reduces the stress in the critical and sensitive beam-to-column welds and reduces the probability of brittle connection failure. Hence, the von Mises stress and *PEEQ* distributions obtained also confirm that the DRBS connection has a relatively superior seismic behavior when strictly low RI_{max} values are desired.

The results for the optimum shapes obtained for connection D-S also showed that the stress concentration shifted towards the second reduced section as RI_{max} decreased and that the decrease in the maximum stress at the beam-column interface was greater for lower RI_{max} values.

In the optimum shapes obtained for connection D-S, both reduced sections entered the plastic range and formed a wide plastic hinge extended across the beam web and flanges. According to Fig. 16, it can be said that creating two reduced sections with appropriate dimensions in the beam flanges leads to a rather uniform distribution of stress.

and equivalent plastic strain across the beam web and flanges at these sections and controls the inelastic stress and strain at the beam-column interface.

4.2.4 Hysteresis Behavior

Since there was almost no overlap between the two reduced sections in the optimum shapes of connection D-S obtained for $0.1 \leq RI_{max} \leq 0.4$, only the hysteresis behavior of these optimum shapes was investigated. Based on the results obtained, the DRBS connection led to hysteresis loops with decreased height, and hence decreased area, similar to the RBS connection when compared to an equivalent non-RBS connection. The reason for such a result is the decrease in the moment transferred to the column face. The results also showed that the decrease in the height of the hysteresis loops lessened as RI_{max} increased.

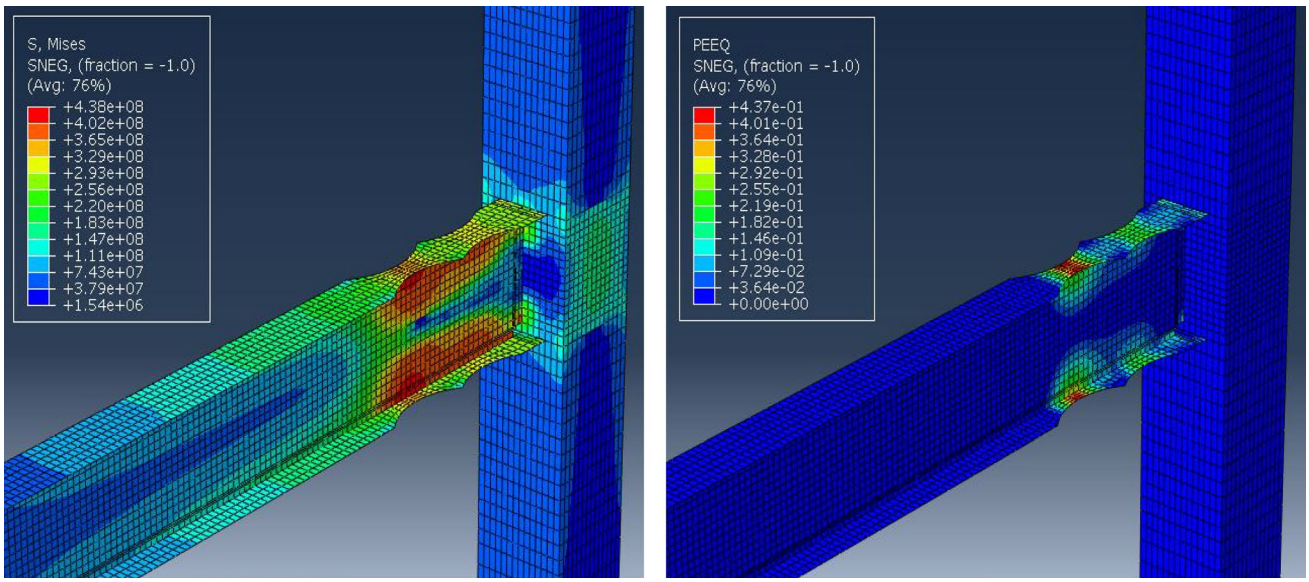

(a) Von Mises stress **(b) *PEEQ***

Fig. 16 The von Mises stress and *PEEQ* distribution in the optimum shape of connection D-S ($RI_{max} = 0.3$)

Furthermore, the hysteresis loops of the optimum shapes of connection D-S plotted before applying the penalty function showed that the DRBS connection did not lead to any decrease in the connection stiffness when compared to the hysteresis data of its equivalent non-RBS connection obtained from Nia et al.'s (2013) study. Such a result suggests that creating two reduced sections in the beam does not have any significant effect on the connection stiffness. Figure 17 shows the hysteresis loops of the optimum shape of connection D-S for $RI_{max} = 0.3$ plotted before and after applying the penalty function as an example.

As can be seen in Fig. 17a, the resulting hysteresis loops were symmetrical, indicating that the optimum shapes of connection D-S had a consistent behavior under the cyclic loading applied. Hence, the results confirmed that the DRBS connection leads to consistent connection behavior under seismic loads. The results obtained showed that the slope in the hysteresis loops obtained did not decrease during the loading cycles.

Therefore, there was no stiffness degradation as the drift applied reached the maximum value of 6%. In addition, there was no decrease in the height of the hysteresis loops as the loading cycles continued indicating that there was also no strength degradation as the drift applied reached the maximum value of 6%. More precisely, the height of the hysteresis loops increased during the loading cycles signifying the strain-hardening behavior in the model considered.

Overall, based on the hysteresis data obtained for the optimum shapes of connection D-S for $0.1 \leq RI_{max} \leq 0.4$, it can be concluded that creating two reduced sections in the beam does not have any effect on stiffness and strength degradation due to seismic loads. However, the resulting decrease in the moment transferred to the column face leads to a decrease in the plastic capacity of the section, which in turn reduces energy absorption.

As can be seen in Fig. 17b, the results obtained showed that the effect of penalty function on hysteresis loops became more significant and resulted in greater decreases in the area of the loops as RI_{max} increased. Also, compared to the hysteresis loops obtained for connection R-S, the effect of the penalty function and hence the decrease in the area of the hysteresis loops was less significant for connection D-S.

4.3 Connections D-M and D-L

In addition to the connection D-S, two larger DRBS connections, namely connections D-M and D-L, were also optimized using the developed CPSO engine to investigate the effect of beam and column size on the optimum shape and seismic performance of the DRBS connection. The optimization procedures for connections D-M and D-L and the limits enforced for the parameters involved were the same as those for connection D-S described in Sect. 4.2 except for the RI_{max} and the corresponding RI_{max}/RI_{final} cases considered, which were selected according to Table 10. The following sections present the optimization results obtained for connections D-M and D-L along with a comparison to those obtained for connection D-S.

4.3.1 Optimum Parameters

The normalized optimum values of the six cut parameters obtained for the RI_{max}/RI_{final} cases considered are presented in Table 11. The CPSO engine performed about 9000 finite element analyses to find these values. According to the results, it can be said that there were no significant differences between the optimum values obtained for connections D-M and D-L and those for connection D-S. In other words,

Table 10 RI_{max} and the corresponding RI_{max}/RI_{final} cases used for in the optimization of connections D-M and D-L

Connection	Case	RI_{max}	RI_{max}/RI_{final}
D-M	1	0.087	0.06
	2	0.262	0.19
	3	0.349	0.25
D-L	1	0.101	0.06
	2	0.304	0.19
	3	0.405	0.25

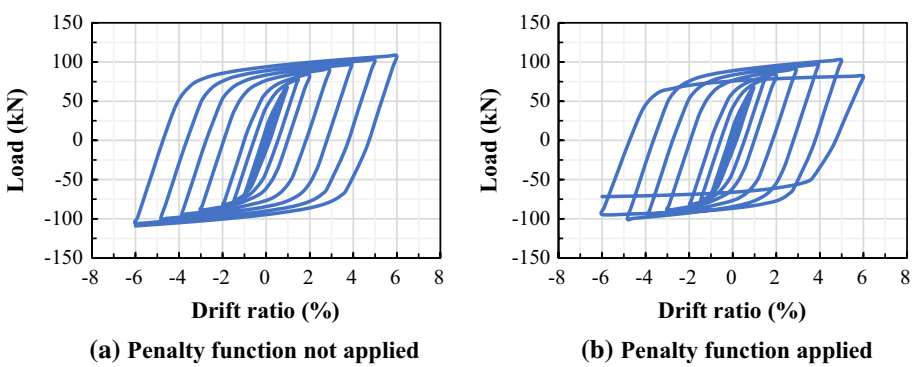

Fig. 17 Hysteresis loops of the optimum shape of connection D-S ($RI_{max} = 0.3$)

Table 11 Normalized optimum cut parameters for connections D-M and D-L

Connection	RI_{max}/RI_{final}	Normalized optimum values					
		a_1	b_1	c_1	a_2	b_2	c_2
D-M	0.06	0.63	0.72	0.25	1.63	0.92	0.34
	0.19	0.68	0.74	0.22	1.70	0.89	0.31
	0.25	0.72	0.79	0.20	1.75	0.80	0.29
D-L	0.06	0.65	0.75	0.25	1.91	0.86	0.35
	0.19	0.68	0.78	0.22	1.96	0.82	0.31
	0.25	0.70	0.81	0.21	1.91	0.81	0.28

Table 12 Percentage difference between the optimum cut parameters; D-M and D-L versus D-S

Connection	RI_{max}/RI_{final}	Difference relative to connection D-S (%)					
		a_1	b_1	c_1	a_2	b_2	c_2
D-M	0.06	−2.61	−2.70	5.26	−2.01	−2.51	2.23
	0.19	1.86	−3.55	3.64	−1.62	−2.35	−1.80
	0.25	3.37	−1.26	−2.10	3.75	−2.75	−4.10
D-L	0.06	0.97	1.83	6.52	4.63	−5.01	3.78
	0.19	2.42	2.03	4.20	3.34	−4.36	1.25
	0.25	0.56	0.32	6.27	−3.57	−1.29	−0.96

the resulting optimum values for these DRBS connections were close in value.

The optimum values presented in Table 11 indicate that the optimum shapes for all RI_{max}/RI_{final} cases considered were in the form of the DRBS connection. By comparing the results presented in Table 11 to those given in Fig. 14, it can be concluded that the nearly all optimum cut parameters for connections D-S, D-M, and D-L followed relatively similar patterns with the change in RI_{max}/RI_{final}. For instance, the optimum parameter a_1 increased with the increase of RI_{max}/RI_{final} in all three models considered. The optimum values obtained for a_1 were also close to each other in the DRBS connections considered. The patterns for all the other optimum parameters except a_2 were also similar to that of a_1. According to Table 11, it is clear that the normalized optimum values for the parameter a_2 differed between the three DRBS connections. Nevertheless, the values obtained for this parameter still indicated a similarity between the results. That is, in all the optimum shapes obtained for the DRBS connections considered, the start of the second reduced section approximately coincided with the end of the first reduced section. Hence, it appears that the beam flange width (b_{bf}) is not a suitable base for the normalization of the parameter a_2.

Table 12 presents the percentage difference between the optimum cut parameters for connections D-M and D-L and the ones obtained for connection D-S. The values in Table 12 indicate that the change in the size of the beam and column sections led to a maximum difference of about 6% in the normalized optimum values compared to the ones obtained for connection D-S. Hence, it can be said that the change in the size of the beam and column sections has a small effect on the optimum values for the cut parameters in the DRBS connection. Therefore, the normalized optimum cut parameters presented in this study can be used to design DRBS connections with beams and columns of different sizes.

Table 13 Optimum values for the distance between the two reduced sections (d) in connections D-M and D-L

Connection	RI_{max}/RI_{final}	d (cm)
D-M	0.06	0.54
	0.19	0.01
	0.25	−1.51
D-L	0.06	1.77
	0.19	0.79
	0.25	−1.56

Similar to connection D-S, the optimum shapes of connections D-M and D-L for $RI_{max}/RI_{final} \leq 0.25$ were in the form of two adjacent reduced sections. The two reduced sections in the optimum shapes obtained did not overlap in nearly all cases considered. The optimum values for the distance between the two reduced sections ($d = a_2 - (a_1 + b_1)$) in connections D-M and D-L are given in Table 13. As mentioned earlier, the negative values calculated for d indicate the amount of overlap between the two reduced sections in each optimum shape obtained.

According to Table 13, in the optimum shapes obtained, the start of the second reduced section approximately coincided with the end of the first reduced section since the

optimum a_2 value was almost equal to the sum of optimum a_1 and b_1 values.

Considering the results obtained, it might seem that the best point for the start of the second reduced section is the end of the first reduced section so that both of them get plasticized simultaneously and form a wide plastic hinge when the seismic loads are applied. However, when the distance between the two reduced sections is considered to be zero, a sharp edge is created at the point where they coincide. This sharp edge results in stress concentration in this critical area. This stress concentration, in turn, provides the conditions for a brittle failure. Hence, considering this possible issue and based on engineering judgment, it can be concluded that the best distance between the two reduced sections in the DRBS connection is approximately 1–2 cm. Therefore, it is better to consider the value of a_2 to be equal to the sum of a_1 and b_1 plus 1–2 cm. In this way, the connection will have better seismic behavior, i.e., greater energy dissipation with less *RI* and *PEEQ* values at the beam-column interface.

4.3.2 RI and PEEQ Values

The optimization results for connection D-S, presented in Sect. 4.2, showed that the DRBS connection led to reduced *RI* and *PEEQ* values at the beam-column interface compared to the simple non-RBS or the RBS connection. To further investigate this topic in the DRBS connections considered, the maximum *RI* and *PEEQ* values at the beam-column interface in the optimum shapes obtained for different RI_{max}/RI_{final} cases are presented in Figs. 18 and 19. According to these two figures, the optimum shapes of connections D-M and D-L behaved in the same way as those of connection D-S. In other words, the maximum *RI* and *PEEQ* values at the beam-column interface decreased with the increase in the RI_{max}/RI_{final}. The maximum *RI* and *PEEQ* values at the beam to column connection were also found to be respectively 1.37 and 0.61 in the simple non-RBS connection equivalent to the connection D-M, and respectively 1.59 and 0.72 in that equivalent to connection D-L. As can be seen in Figs. 18 and 19, the maximum *RI* and *PEEQ* values in the optimum shapes of connections D-M and D-L were significantly lower than those measured in their equivalent simple non-RBS connections. Thus, the DRBS connection led to improved performance and lowered brittle failure potential.

4.3.3 PEEQ Distribution

The *PEEQ* distribution in the optimum shapes obtained for connections D-M and D-L indicated that the maximum *PEEQ* values occurred at the reduced sections. Accordingly, the plastic hinge location also shifted away from the beam-column interface. More precisely, the results showed that both of the reduced sections in optimum designs obtained entered the plastic range and formed a wide plastic hinge extended across the beam web and flanges. Shifting of the plastic strain concentration away from the beam-column interface prevents the damage to the beam-to-column welds in this critical and sensitive area and thus decreases the probability of brittle connection failure. Furthermore, the results showed that similar to connection D-S, the optimum cut parameters obtained for the reduced sections in connections D-M and D-L resulted in a relatively uniform distribution of *PEEQ* across the beam web and flanges and reduced inelastic strain at the beam-column interface.

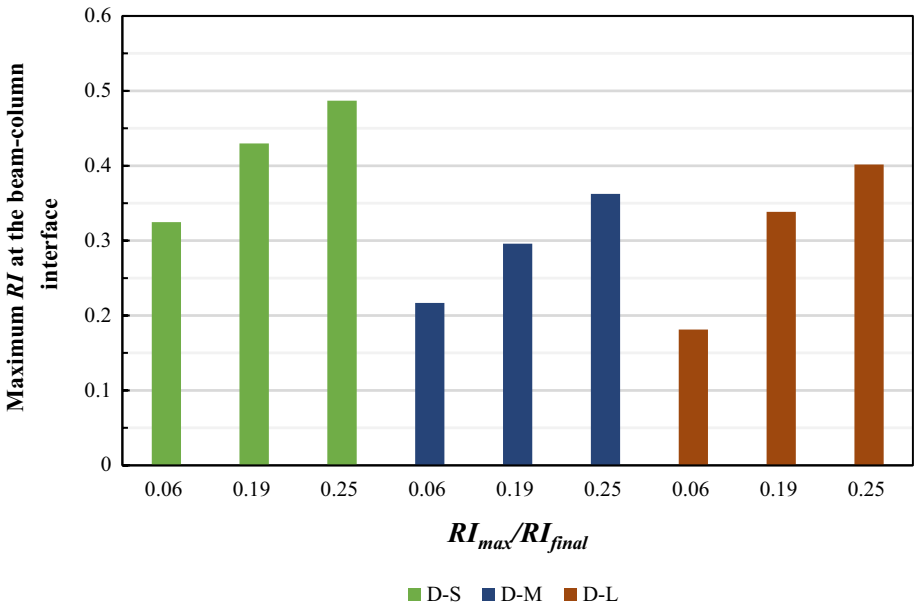

Fig. 18 Maximum *RI* values at the beam-column interface in the optimum shapes of connections D-S, D-M, and D-L for different RI_{max}/RI_{final} cases

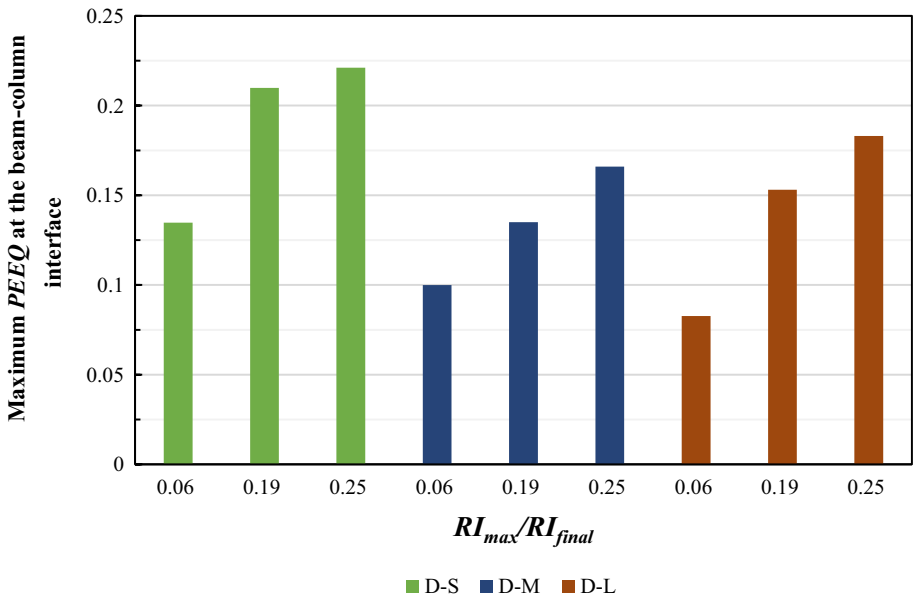

Fig. 19 Maximum *PEEQ* values at the beam-column interface in the optimum shapes of connections D-S, D-M, and D-L for different RI_{max}/RI_{final} cases

Table 14 Improvements of optimum design determined in this research with respect to the original DRBS connection (Morshedi et al., 2017)

RI_{max}/RI_{final}	Percentage increase in the objective function (%)	Percentage decrease in *RI* (%)	Percentage decrease in *PEEQ* (%)
0.06	28	36	38
0.19	20	32	33
0.25	15	23	25

4.3.4 Comparison Against the Original DRBS Connection

The improvements in terms of percentage increase in the objective function and percentage decreases in the *RI* and *PEEQ* index, resulting from the optimized connection design obtained in this study, compared to the original DRBS connection, proposed by Morshedi et al. (2017), are presented in Table 14. According to this table, it is clear that the resulting optimum connection design parameters determined in this paper led to up to a 28% increase in the objective function (energy dissipation) and up to respectively 36% and 38% decreases in the *RI* and *PEEQ* index, which indicates noticeable seismic performance enhancements with respect to the original DRBS connection.

5 Conclusions

In this study, an optimization engine was developed utilizing the chaotic particle swarm optimization (CPSO) technique and finite element modeling to optimize the newly proposed double reduced beam section (DRBS) connection and provide the optimum cut parameters for the best seismic performance. In order to confirm the accuracy of the developed CPSO engine, and to obtain data for comparison, it was first tested on a conventional RBS connection. The CPSO engine was then utilized to optimize DRBS connections of three different sizes and find the optimum values for all of the cut parameters involved. Based on the results obtained, the seismic performance of the DRBS connection was investigated compared to the conventional RBS connection. Also, the results were employed to evaluate the effect of the beam and column section size on the optimum shape and the seismic performance of the DRBS connection. The criteria used for assessing the seismic performance of connections included the total energy dissipated during the loading (the objective function chosen), the rupture index (*RI*), and the equivalent plastic strain (*PEEQ*). The following conclusions summarize the results obtained:

(1) Based on the results, the optimum values obtained for the cut parameters in the RBS connection were within the limits defined by ANSI/AISC 358-16 (2016b) when the desired upper limit for *RI* (RI_{max}) was selected between 0.4 and 0.9 ($0.25 \le RI_{max}/RI_{final} \le 0.57$). For $RI_{max} \le 0.4$, the reduction in the flange cross-sectional area exceeded the limit defined by ANSI/AISC 358-16 (2016b). For $RI_{max} \ge 0.9$, the optimum shape tended towards the simple non-RBS connection.

(2) The results showed that the optimum shape of the DRBS connection is dependent on the RI_{max}/RI_{final} value considered. The optimum shape was found to be in the form of two adjacent reduced sections for $RI_{max}/RI_{final} \le 0.25$. However, for $RI_{max}/RI_{final} > 0.25$,

the two reduced sections overlapped, and the optimum shape tended towards the RBS connection.

(3) There was almost no overlap between the two reduced sections in the optimum shapes of the DRBS connection obtained for $RI_{max} \leq 0.4$. The optimum distance was found to be within the interval [− 1.5, 1.8] cm, where negative values indicate the amount of overlap between the two reduced sections. Nonetheless, based on engineering judgment, the best value for this parameter seems to be equal to 1 or 2 cm to avoid creating sharp edges leading to stress concentration, which can impede the balanced plasticization of the reduced sections and increase the risk of brittle connection failure.

(4) The optimum shapes of DRBS connection obtained for $RI_{max}/RI_{final} \leq 0.25$ led to up to 39% higher objective function values compared to those of the RBS connection. In other words, in the optimum DRBS connections presented, application of the penalty function led to smaller decreases in the area of the hysteresis loops.

(5) The optimum shapes of DRBS connection obtained for $RI_{max}/RI_{final} \leq 0.25$ led to up to respectively 50% and 55% lower *RI* and *PEEQ* values at the beam-column interface compared to those of the RBS connection. Such significant improvements in *RI* and *PEEQ* values result in a lower potential for brittle failure and enhance the efficiency of the beam-to-column connections in steel moment frames.

(6) The optimum shapes of the DRBS connection obtained for $RI_{max}/RI_{final} > 0.25$ exhibited no improvements in terms of *RI* and *PEEQ* at the beam-column interface. Hence, the DRBS connection does not appear to be the superior design for such RI_{max}/RI_{final} cases.

(7) The von Mises stress and *PEEQ* distributions in the optimum shapes obtained for $RI_{max}/RI_{final} \leq 0.25$ confirmed that utilizing the DRBS connection shifts the plastic hinge away from the beam-column interface and to the two reduced sections. In the optimized DRBS connections, both the reduced sections underwent plasticization, resulting in a wide plastic hinge extended in the beam web and flanges.

(8) The results showed that changing the size of the beam and column sections does not lead to any significant change in the optimal shape of the beam flange cut. The maximum difference between the optimal beam section parameters for the beam and columns in this study for different connection sizes was about 6%.

(9) The optimum connection design parameters determined in this paper led to up to a 28% increase in the objective function (energy dissipation) and up to respectively 36% and 38% decreases in the *RI* and *PEEQ* index with respect to the original DRBS connection proposed by Morshedi et al. (2017), which indicates noticeable seismic performance enhancements.

This study presented the numerical analysis and optimization of the newly proposed DRBS connection based on the CPSO method. Results obtained in this paper and those from previously conducted theoretical and numerical studies indicate that this design provides improved seismic behavior and could be utilized as an enhanced alternative to the conventional RBS connection. Nonetheless, it should be emphasized that experimental research is still necessary to evaluate the actual seismic performance of DRBS connections more comprehensively. Hence, further studies in this field can focus on experimental testing of DRBS connection specimens to observe the intended plastic hinge formation in frames incorporating such connections and confirm the optimum design parameters. The DRBS connection could be added to the category of prequalified steel moment connections and readily used in the industry in case future experimental research data confirm its promising performance suggested by theoretical and numerical studies.

Funding This research did not receive any specific Grant from funding agencies in the public, commercial, or not-for-profit sectors.

Declarations

Conflict of interest The authors declare that they have no known competing financial interests or personal relationships that could have appeared to influence the work reported in this paper.

References

Altinoz, O. T., Yilmaz, A. E., & Weber, G. W. (2010). Chaos particle swarm optimized PID controller for the inverted pendulum system. In *2nd international conference on engineering optimization*.

American Institute of Steel Construction. (2016a). *ANSI/AISC 341-16 seismic provisions for structural steel buildings*. American Institute of Steel Construction (AISC).

American Institute of Steel Construction. (2016b). *ANSI/AISC 358-16 prequalified connections for special and intermediate steel moment frames for seismic applications*. American Institute of Steel Construction (AISC).

American Institute of Steel Construction. (2016c). *ANSI/AISC 360-16 specification for structural steel buildings*. American Institute of Steel Construction (AISC).

American Welding Society. (2016). *ANSI/AWS D1.8/D1.8M:2016 structural welding code-seismic supplement*. American Welding Society (AWS).

Chen, C. C., Lin, C. C., & Lin, C. H. (2006). Ductile moment connections used in steel column-tree moment-resisting frames. *Journal of Constructional Steel Research, 62*(8), 793–801. https://doi.org/10.1016/j.jcsr.2005.11.012

Chen, C. C., Lin, C. C., & Tsai, C. L. (2004). Evaluation of reinforced connections between steel beams and box columns. *Engineering Structures, 26*(13), 1889–1904. https://doi.org/10.1016/j.engstruct.2004.06.017

Chen, S. J., & Tu, C. T. (2004). Experimental study of jumbo size reduced beam section connections using high-strength steel.

Journal of Structural Engineering, 130(4), 582–587. https://doi.org/10.1061/(ASCE)0733-9445(2004)130:4(582)

Chen, S. J., Yeh, C. H., & Chu, J. M. (1996). Ductile steel beam-to-column connections for seismic resistance. *Journal of Structural Engineering, 122*(11), 1292–1299. https://doi.org/10.1061/(ASCE)0733-9445(1996)122:11(1292)

Collin, J. M., Parenteau, T., Mauvoisin, G., & Pilvin, P. (2009). Material parameters identification using experimental continuous spherical indentation for cyclic hardening. *Computational Materials Science, 46*(2), 333–338. https://doi.org/10.1016/j.commatsci.2009.03.016

Dos Santos, C. L., & Mariani, V. C. (2009). A novel chaotic particle swarm optimization approach using Hénon map and implicit filtering local search for economic load dispatch. *Chaos Solitons & Fractals, 39*(2), 510–518. https://doi.org/10.1016/j.chaos.2007.01.093

Eberhart, R., & Kennedy, J. (1995). A new optimizer using particle swarm theory. In *MHS'95 proceedings of the sixth international symposium on micro machine and human science* (pp. 39–43). Institute of Electrical and Electronics Engineers (IEEE). https://doi.org/10.1109/MHS.1995.494215

El-Bahey, S., & Bruneau, M. (2012). Bridge piers with structural fuses and bi-steel columns I: Experimental testing. *Journal of Bridge Engineering, 17*(1), 25–35. https://doi.org/10.1061/(ASCE)BE.1943-5592.0000234

El-Tawil, S., Vidarsson, E., Mikesell, T., & Kunnath, S. K. (1999). Inelastic behavior and design of steel panel zones. *Journal of Structural Engineering, 125*(2), 183–193. https://doi.org/10.1061/(ASCE)0733-9445(1999)125:2(183)

Engelhardt, M. D., Winneberger Zekany, A. J., & Potyraj, T. J. (1998). Experimental investigation of dogbone moment connections. *Engineering Journal, 35*, 128–139.

Fanaie, N., Faegh, S. S., & Partovi, F. (2019). An improved and innovative formulation for calculating amplified elastic story drift induced by RBS connections in steel moment frames. *Journal of Constructional Steel Research, 160*, 510–527. https://doi.org/10.1016/j.jcsr.2019.06.003

Federal Emergency Management Agency. (2000). *FEMA 350 recommended seismic design criteria for new steel moment frame buildings*. Federal Emergency Management Agency (FEMA).

Foraboschi, P. (2016). Versatility of steel in correcting construction deficiencies and in seismic retrofitting of RC buildings. *Journal of Building Engineering, 8*, 107–122. https://doi.org/10.1016/j.jobe.2016.10.003

Foraboschi, P. (2019). Lateral load-carrying capacity of steel columns with fixed-roller end supports. *Journal of Building Engineering, 26*, 100879. https://doi.org/10.1016/j.jobe.2019.100879

Foraboschi, P. (2020). Predictive formulation for the ultimate combinations of axial force and bending moment attainable by steel members. *International Journal of Steel Structures*. https://doi.org/10.1007/s13296-020-00316-6

Gharebaghi, S. A., & Zangooeia, E. (2017). Chaotic particle swarm optimization in optimal active control of shear buildings. *Structural Engineering and Mechanics, 61*(3), 347–357. https://doi.org/10.12989/sem.2017.61.3.347

Kim, H. H., Choi, J. Y., & Park, S. C. (2017). Tire mixing process scheduling using particle swarm optimization. *Computers & Industrial Engineering, 110*, 333–343. https://doi.org/10.1016/j.cie.2017.06.012

Mahin, S. A. (1998). Lessons from damage to steel buildings during the Northridge earthquake. *Engineering Structures, 20*(4–6), 261–270. https://doi.org/10.1016/S0141-0296(97)00032-1

Morshedi, M. A., Dolatshahi, K. M., & Maleki, S. (2017). Double reduced beam section connection. *Journal of Constructional Steel Research, 138*, 283–297. https://doi.org/10.1016/j.jcsr.2017.07.013

Nia, Z. S., Ghassemieh, M., & Mazroi, A. (2013). WUF-W connection performance to box column subjected to uniaxial and biaxial loading. *Journal of Constructional Steel Research, 88*, 90–108. https://doi.org/10.1016/j.jcsr.2013.04.008

Parsopoulos, K. E., Plagianakos, V. P., Magoulas, G. D., & Vrahatis, M. N. (2001). Improving the particle swarm optimizer by function "stretching". In *Advances in convex analysis and global optimization* (pp. 445–457). Springer. https://doi.org/10.1007/978-1-4613-0279-7_28

Plumier, A. (1990). New idea for safe structures in seismic zones. In *IABSE symposium—Mixed structures including new materials*. International Association for Bridge and Structural Engineering.

Popov, E. P., Balan, T. A., & Yang, T. S. (1998). Post-Northridge earthquake seismic steel moment connections. *Earthquake Spectra, 14*(4), 659–677. https://doi.org/10.1193/1.1586021

Rahnavard, R., Hassanipour, A., & Siahpolo, N. (2015). Analytical study on new types of reduced beam section moment connections affecting cyclic behavior. *Case Studies in Structural Engineering, 3*, 33–51. https://doi.org/10.1016/j.csse.2015.03.001

Shi, Y., & Eberhart, R. (1998). A modified particle swarm optimizer. In *1998 IEEE international conference on evolutionary computation proceedings IEEE world congress on computational intelligence, Cat no. 98TH8360* (pp. 69–73). Institute of Electrical and Electronics Engineers (IEEE). https://doi.org/10.1109/ICEC.1998.699146

Sophianopoulos, D. S., & Deri, A. E. (2011). Parameters affecting response and design of steel moment frame reduced beam section connections: An overview. *International Journal of Steel Structures, 11*(2), 133–144. https://doi.org/10.1007/s13296-011-2003-5

Uang, C. M., & Fan, C. C. (2001). Cyclic stability criteria for steel moment connections with reduced beam section. *Journal of Structural Engineering, 127*(9), 1021–1027. https://doi.org/10.1061/(ASCE)0733-9445(2001)127:9(1021)

Zhang, X., Ricles, J. M., Lu, L. W., & Fisher, J. W. (2004). Analytical and experimental studies on seismic behavior of deep column-to-beam welded reduced beam section moment connections. In *Proceedings of the 13th world conference on earthquake engineering*.